# SN 2017ckj: A linearly declining Type IIb supernova with a relatively massive hydrogen envelope

L.-H. Li<sup>1,2,3</sup>, S. Benetti<sup>4</sup>, Y.-Z. Cai<sup>1,2,\*</sup>, B. Wang<sup>1,2,\*\*</sup>, A. Pastorello<sup>4</sup>, N. Elias-Rosa<sup>4,5</sup>, A. Reguitti<sup>4,17</sup>, L. Borsato<sup>4</sup>, E. Cappellaro<sup>4</sup>, A. Fiore<sup>4,6</sup>, M. Fraser<sup>7</sup>, M. Gromadzki<sup>8</sup>, J. Harmanen<sup>9</sup>, J. Isern<sup>5, 10, 11</sup>, T. Kangas<sup>12, 9</sup>, E. Kankare<sup>9</sup>, P. Lundqvist<sup>13</sup>, S. Mattila<sup>9, 14</sup>, P. Ochner<sup>4, 15</sup>, Z.-H. Peng<sup>16</sup>, T. M. Reynolds<sup>9, 18, 19</sup>, I. Salmaso<sup>20</sup>, S. Srivastav<sup>21</sup>, M. D. Stritzinger<sup>22</sup>, L. Tomasella<sup>4</sup>, G. Valerin<sup>4</sup>, Z.-Y. Wang<sup>23,24</sup>, J.-J. Zhang<sup>1,2</sup>, and C.-Y. Wu<sup>1,2,3</sup>

(Affiliations can be found after the references)

Received September xx, 2025; accepted March xx, 2025

#### **ABSTRACT**

We present optical observations of the Type IIb supernova (SN) 2017ckj, covering approximately 180 days after the explosion. Its early-time multi-band light curves display no clear evidence of a shock-cooling tail, resembling the behavior of SN 2008ax. The V-band light curve exhibits a short rise time of about 5 days and reaches an absolute peak magnitude of  $M_V = -18.58 \pm 0.17$  mag. The late-time multi-band light curves reveal a linear decline. We modelled the bolometric light curve of SN 2017ckj to constrain the progenitor and the explosion parameters. We estimated a total mass of  $^{56}$ Ni synthesized by SN 2017ckj of  $M_{\text{Ni}} = 0.21^{+0.05}_{-0.03} M_{\odot}$ , with a massive H-rich envelope of  $M_{\text{env}} = 0.4^{+0.1}_{-0.1} M_{\odot}$ . Both the  $^{56}$ Ni mass a linear decline. We modelled the bolometric light curve of NN 2017 key to constraint use programment and use and the contrast, some population synthesized by SN 2017ckj of M<sub>NS</sub> = 0.21<sup>+0.05</sup><sub>-0.05</sub> M<sub>☉</sub>, with a massive H-rich envelope of M<sub>em</sub> = 0.4<sup>+0.1</sup><sub>-0.1</sub> M<sub>☉</sub>. Both the <sup>56</sup>Ni mass and the envelope mass of SN 2017ckj are higher than those of typical SNe Ilb, in agreement with its peculiar light curve evolution. The early-time spectra of SN 2017ckj are higher than those of typical SNe Ilb, in agreement with its peculiar light curve evolution. The early-time spectra of SN 2017ckj are higher than those of typical SNe Ilb, in agreement with its peculiar light curve evolution. The early-time spectra of SN 2017ckj are higher than those of typical SNe Ilb, in agreement with its peculiar light curve evolution. The early-time spectra of SN 2017ckj are higher than those of typical SNe Ilb, in agreement with its peculiar light curve evolution. The early-time spectra of SN 2017ckj are higher than those of typical SNe Ilb, in agreement with its peculiar light curve evolution. The early-time spectra of SN 2017ckj are higher than those of typical SNe Ilb, in agreement with its peculiar light curve evolution. The early-time spectra of SN 2017ckj are higher than those of SN 2017ckj and the envelope of the strong higher than those of SN 2017ckj and the envelope of the strong higher than the spectrum dominated by hard and the emission lines. The earliest spectrum at around 139 days does not show a distinct decline in the strength of the expection mas-loss rate or ~ 3.4 × 10<sup>-4</sup> M<sub>☉</sub> yr<sup>1</sup>. At 10<sup>-4</sup> M<sub>☉</sub> yr<sup>1</sup>. At 10<sup>-4</sup> M<sub>☉</sub> yr<sup>1</sup> At 10<sup>-4</sup> M<sub>☉</sub> yr<sup></sup>

contrast, some population synthesis studies have indicated that stars evolving in close binary systems can produce a sufficient number of SE-SNe (e.g. Yoon & Cantiello 2010; Eldridge et al. 2013; Fang et al. 2019).

The various subclasses of SE-SNe originate from progenitors that have undergone different degrees of envelope stripping before CC, and exhibit diverse spectral features throughout their spectral evolution (e.g. Prentice & Mazzali 2017). If all or the majority of hydrogen is removed from the outer envelope, an Hpoor SN Ib/c will occur. As a consequence, SNe Ib/c lack any prominent hydrogen features within their spectral evolution and

1988). Subsequently, SN 1993J was discovered on 28.9 March 1993 in the nearby galaxy M81 (Ripero et al. 1993). SN 1993J has been extensively studied and is considered a prototypical example of SNe IIb (e.g. Woosley et al. 1994; Filippenko & Matheson 2003).

The double-peaked light curves, primarily observed in the optical bands, have been reported in a few SNe IIb, such as SN 1993J (e.g. Richmond et al. 1994), SN 2011dh (e.g. Sahu et al. 2013; Ergon et al. 2014; Marion et al. 2014; Ergon et al. 2015), SN 2011fu (Morales-Garoffolo et al. 2015), SN 2016gkg (Bersten et al. 2018), SN 2024uwg (Subrayan et al. 2025), and SN 2024aecx (Zou et al. 2025). These SNe IIb are characterized by an initial decline due to shock-cooling, followed by a

Corresponding authors: caiyongzhi@ynao.ac.cn (CYZ)

<sup>\*\*</sup> wangbo@ynao.ac.cn (WB)

second peak powered by the radioactive decay of <sup>56</sup>Ni, which typically dominates the late-time luminosity evolution. However, some SNe IIb with continuous early-time coverage, such as SN 2008ax (e.g. Pastorello et al. 2008; Taubenberger et al. 2011) and SN 2020acat (Medler et al. 2022), do not display the initial shock-cooling tail prior to the <sup>56</sup>Ni-powered peak. This observational diversity suggests the existence of two distinct categories of SN IIb progenitors: extended and compact (e.g. Chevalier & Soderberg 2010; Branch & Wheeler 2017). Extended progenitors with large H-rich envelopes exhibit a noticeable shock-cooling tail after the explosion, whereas compact progenitors show no such feature.

SN progenitor constraints have been derived through deep pre- and post-explosion imaging with high spatial resolution. primarily using data obtained by the Hubble Space Telescope (HST) and other ground- or space-based facilities. To date, some SNe IIb progenitors have been identified: SN 1993J (e.g. Aldering et al. 1994; Maund et al. 2004), SN 2008ax (Crockett et al. 2008; Folatelli et al. 2015), SN 2011dh (Van Dyk et al. 2011), SN 2013df (Van Dyk et al. 2014), SN 2016gkg (Kilpatrick et al. 2017; Tartaglia et al. 2017), SN 2017gkk (Niu et al. 2024), and SN 2024abfo (Reguitti et al. 2025; Niu et al. 2025). The progenitor of SN 1993J was identified in pre-explosion imaging as a K-type supergiant (Van Dyk et al. 2002). A B-type companion star was later detected, providing direct evidence that SN 1993J originated from a binary system undergoing masstransfer phase (Maund et al. 2004). Yellow supergiant (YSG) progenitors with an initial mass of  $\sim 10-17 \, M_{\odot}$  have been identified for SN 2011dh, SN 2013df, SN 2016gkg, SN 2017gkk, and SN 2024abfo (e.g. Maund et al. 2011; Bersten et al. 2012; Maeda et al. 2015; Kilpatrick et al. 2022; Niu et al. 2024; Reguitti et al. 2025). In contrast, the progenitor of SN 2008ax is likely a highly stripped star (a low-mass analogue of a WR star) in a binary system (Crockett et al. 2008; Folatelli et al. 2015). Another SN IIb, SN 2013cu, was suggested to have a Wolf–Rayet–like progenitor undergoing intense mass loss shortly before the explosion, based on the detection of narrow high-ionization emission lines in its early flash spectrum (Gal-Yam et al. 2014).

In this paper, we present photometric and spectroscopic observations of SN 2017ckj, a peculiar and luminous SN IIb characterized by a linear decline in its multi-band light curves. In Section 2, we report the distance, extinction, and reddening associated with the host galaxy of SN 2017ckj. The photometric and spectroscopic analyses are presented in Sections 3 and 4, respectively. Finally, the discussions are presented in Section 5, and the concluding remarks are provided in Section 6. Additionally, we present the supplementary figure in Appendix A, the data reduction techniques in Appendix B, and the relevant data tables in Appendix C.

# 2. Basic target information

SN 2017ckj was discovered by the Asteroid Terrestrial-impact Last Alert System (ATLAS; Tonry et al. 2018a,b; Smith et al. 2020) on 26.55 March 2017 (epoch corresponding to MJD = 57838.55; UT dates are used throughout this paper), at an ATLAS cyan-filter (c) brightness c = 17.81 mag (Tonry et al. 2017). The last non-detection by ATLAS was on 22.62 March 2017 (MJD = 53834.62) in the c-band, with an estimated limit of 19.53 mag. Soon after its discovery, it was classified as a CC SN event by Tomasella et al. (2017) and Benetti (2017) in the framework of the Asiago Transient Classification Program (Tomasella et al. 2014). Its J2000 coordinates are  $\alpha = 16^{\rm h}09^{\rm m}44.400^{\rm s}$ ,  $\delta = +48^{\circ}02'07.26''$ , placing it 2.01" south and 10.70" east of

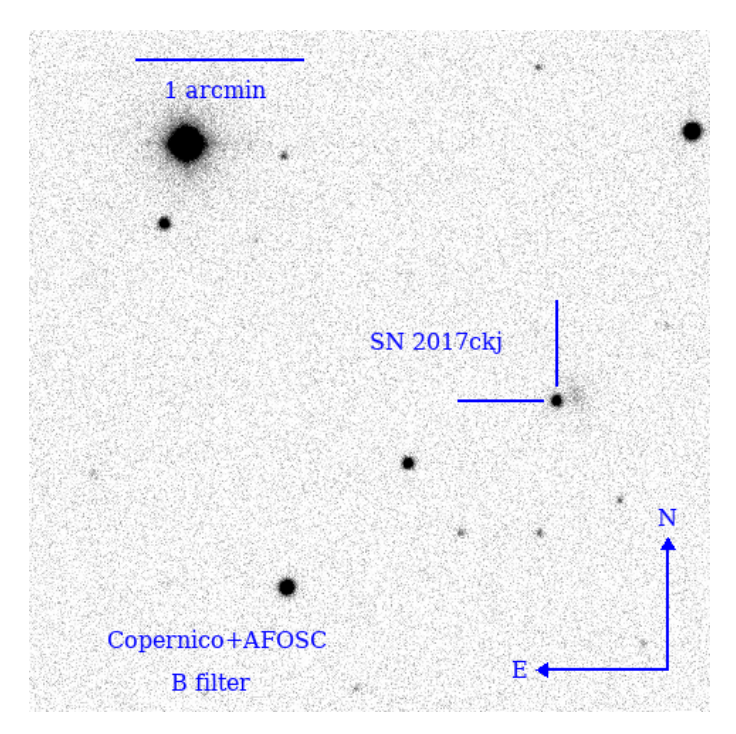


Fig. 1: Image of the location of SN 2017ckj, taken on 29 March 2017 by the Copernico telescope with the *B*-filter. The orientation and scale of the images are reported.

Table 1: Summary of the basic properties of SN 2017ckj

RA (J2000)	16:09:44.40
DEC (J2000)	+48:02:07.26
Host Galaxy	WISEA J160943.68+480209.2
Redshift z	$0.037077 \pm 0.000014$
$\mu$	$35.99 \pm 0.15 \mathrm{mag}$
d	$158.1 \pm 11.1 \mathrm{Mpc}$
$E(B-V)_{\mathrm{Gal}}^{1}$	0.013 mag
$E(B-V)_{ m host}$	$\sim 0  \mathrm{mag}$
Last Non-Detection (MJD)	57834.62
First Discovery (MJD)	57838.55
Midpoint epoch (MJD)	$57836.6 \pm 2.0$
Estimated Explosion (MJD) <sup>2</sup>	$57837.1 \pm 0.1$

Notes: 1. Retrieved from NASA/IPAC NED (Schlafly & Finkbeiner 2011).

2. Estimated from the shock-cooling light curve fitting.

the core of the host galaxy WISEA J160943.68+480209.2 (also named SDSS J160943.66+480209.4; Cutri et al. 2013). The location of SN 2017ckj within the host galaxy is illustrated in Figure 1, and the basic properties of SN 2017ckj are shown in Table 1.

The redshift of the host galaxy of SN 2017ckj is  $0.037077 \pm 0.000014$ . Adopting a standard cosmology (H<sub>0</sub> = 73 ±  $5 \, \mathrm{kms^{-1} \, Mpc^{-1}}$ ,  $\Omega_M$  = 0.27 and  $\Omega_\Lambda$  = 0.73; Spergel et al. 2007) and corrected for the Virgo Cluster, the Great Attractor, and the Shapley supercluster influence, we obtained a Hubble flow distance  $d = 158.1 \pm 11.1 \, \mathrm{Mpc}$  and distance modulus  $\mu = 35.99 \pm 0.15 \, \mathrm{mag}$  for WISEA J160943.68+480209.2 <sup>1</sup> (Albareti et al. 2017). Regarding the interstellar reddening, we adopt

https://ned.ipac.caltech.edu

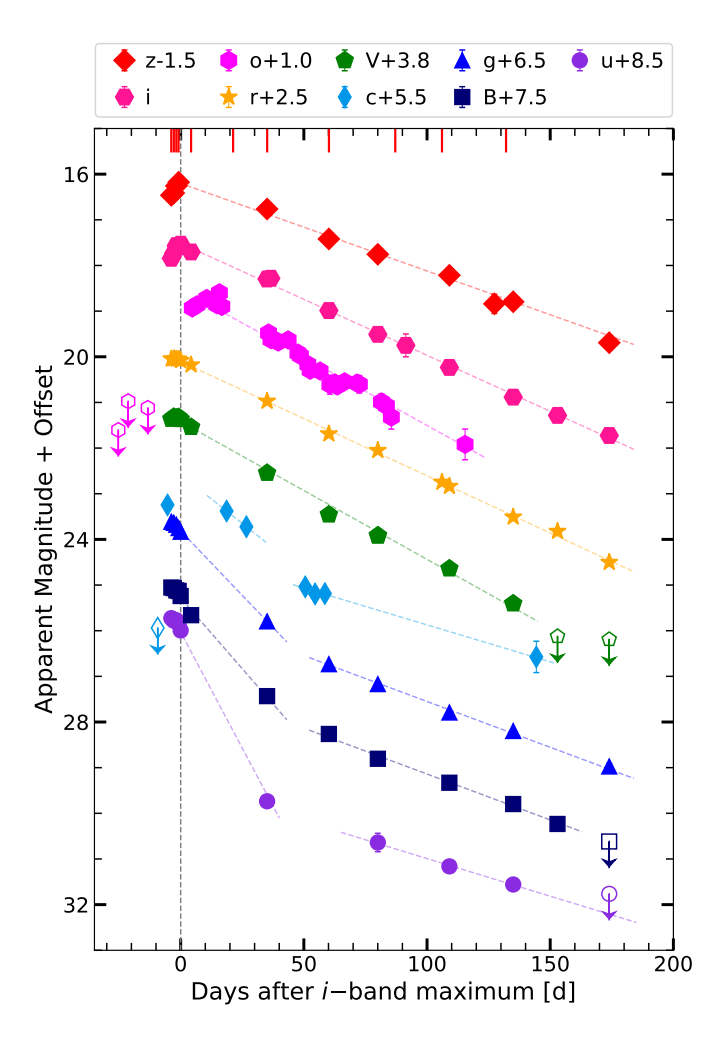


Fig. 2: Multi-band light curves of SN 2017ckj. A dashed vertical line is used to visually represent the reference epoch (MJD = 57843.9), which corresponds to the *i*-band observation maximum. The linear fit is applied to the light curve in each band, as indicated by the dashed lines. The epochs of our spectra are marked with vertical solid red lines on the top. In most cases, the errors associated with the magnitudes are smaller than the plotted symbol sizes.

 $E(B-V)_{\rm Gal}=0.013$  mag for the Galactic reddening contribution (Schlafly & Finkbeiner 2011), retrieved via the NASA/IPAC Extragalactic Database (NED), assuming a reddening law with  $R_V=3.1$  (Cardelli et al. 1989). No strong, narrow interstellar Na1D  $\lambda\lambda$ 5890,5896 absorption lines were detected at the redshift of the host galaxy. The lack of strong Na1D lines, along with the position of SN 2017ckj relative to its host galaxy, implies that the dust extinction of the host galaxy  $E(B-V)_{\rm host}$  is negligible. Therefore, we adopt  $E(B-V)_{\rm total}=0.013$  mag as the total reddening towards SN 2017ckj.

# 3. Photometry

# 3.1. Apparent light curves

We conducted continuous photometric observations of SN 2017ckj for about six months after its discovery. The multi-band optical light curves of SN 2017ckj are shown in Figure 2. For SN 2017ckj, the last non-detection  $t_l$  occurred on MJD = 57834.62 with an estimated limit of 19.53 mag

Table 2: Decline rates (in mag /100 d) of the multi-band light curves of SN 2017ckj.

Filter	$\gamma_{0-40}$	γ <sub>40-200</sub>			
u	10.16±0.27	1.65±0.40			
В	$6.19 \pm 0.11$	$2.01 \pm 0.11$			
g	$5.65 \pm 0.08$	$2.01 \pm 0.04$			
c	$4.28\pm0.59$	$1.62 \pm 0.38$			
Filter	γ <sub>0</sub> –200				
V	3.02±0.02				
r	$2.50\pm0.01$				
0	$2.99 \pm 0.09$				
i	$2.47 \pm 0.02$				
Z	$1.92 \pm 0.03$				

in the ATLAS c-band, while the first detection epoch  $t_d$  is MJD = 57838.55 with c = 17.81 mag (Tonry et al. 2017). The midpoint between  $t_l$  and  $t_d$  provides a rough estimate of the explosion epoch of MJD =  $57836.6 \pm 2.0$ . To more accurately determine the explosion epoch, we fit the early-time light curve using the Light Curve Fitting package <sup>2</sup> (Hosseinzadeh et al. 2024), which implements the shock-cooling model of Sapir & Waxman (2017). This package has been applied to shock-cooling analyses of several SNe, including SN 2016gkv (Hosseinzadeh et al. 2018), SN 2021yja (Hosseinzadeh et al. 2022), and SN 2023ixf (Hosseinzadeh et al. 2023). We ran 100 walkers for 5000 steps until convergence, which was confirmed through visual inspection of the MCMC chains. The best-fit light curve, along with the posterior distributions and parameter correlations, is shown in Figure A.1 of Appendix A. The fitting yields a more precise explosion epoch of MJD =  $57837.1 \pm 0.1$ , which is adopted in the following analysis.

In Figure 2, the *B*, *V* and *i*-bands exhibit a visible peak in their light curves. To estimate the peak magnitude of SN 2017ckj, we performed a Markov Chain Monte Carlo (MCMC) fit using a second-order polynomial to model the early-time BVi-band light curves. The peak of the *B*-band is  $17.36 \pm 0.02$  mag at MJD =  $57840.20 \pm 1.6$ . The peak of the *V*-band is  $17.54 \pm 0.03$  mag at MJD =  $57842.1 \pm 1.5$ . The peak of the *i*-band is  $17.52 \pm 0.02$  mag at MJD =  $57844.7 \pm 0.2$ . Note that the ATLAS *o*-band data exhibits a slight upward trend around 5-10 d after the *i*-band maximum, likely attributable to the increasing contribution from the emission around H $\alpha$  feature, which lies within the spectral coverage of the *o*-band.

Using the previously fitted peak time, the V-band rise time of SN 2017ckj is approximately 5 d, which is faster than all SNe IIb. Pessi et al. (2019) analyzed the light curve morphology of 22 SNe IIb and reported a weighted average rise time of 19.0  $\pm$  1.8 d. SN 2004ff, a type IIb SN with a rapid B-band rise time of 9.4  $\pm$  4.0 d, made it one of the fastest-rising SNe IIb (Stritzinger et al. 2018). Similarly, SN 2013cu had a fast r-band rise time of  $\sim$  10 d and has been suggested to originate from a Wolf–Rayet-like progenitor (Gal-Yam et al. 2014). The rapid rise time of SN 2017ckj indicates that it has originated from a progenitor with unusual characteristics.

In Figure 2, after reaching peak brightness, the multi-band light curves of SN 2017ckj exhibit a clear linear decline, particularly in *riz*-bands. However, the decline rates show noticeable variations around 40 days, especially in the *uBg*-bands.

<sup>2</sup> https://github.com/griffin-h/lightcurve\_fitting

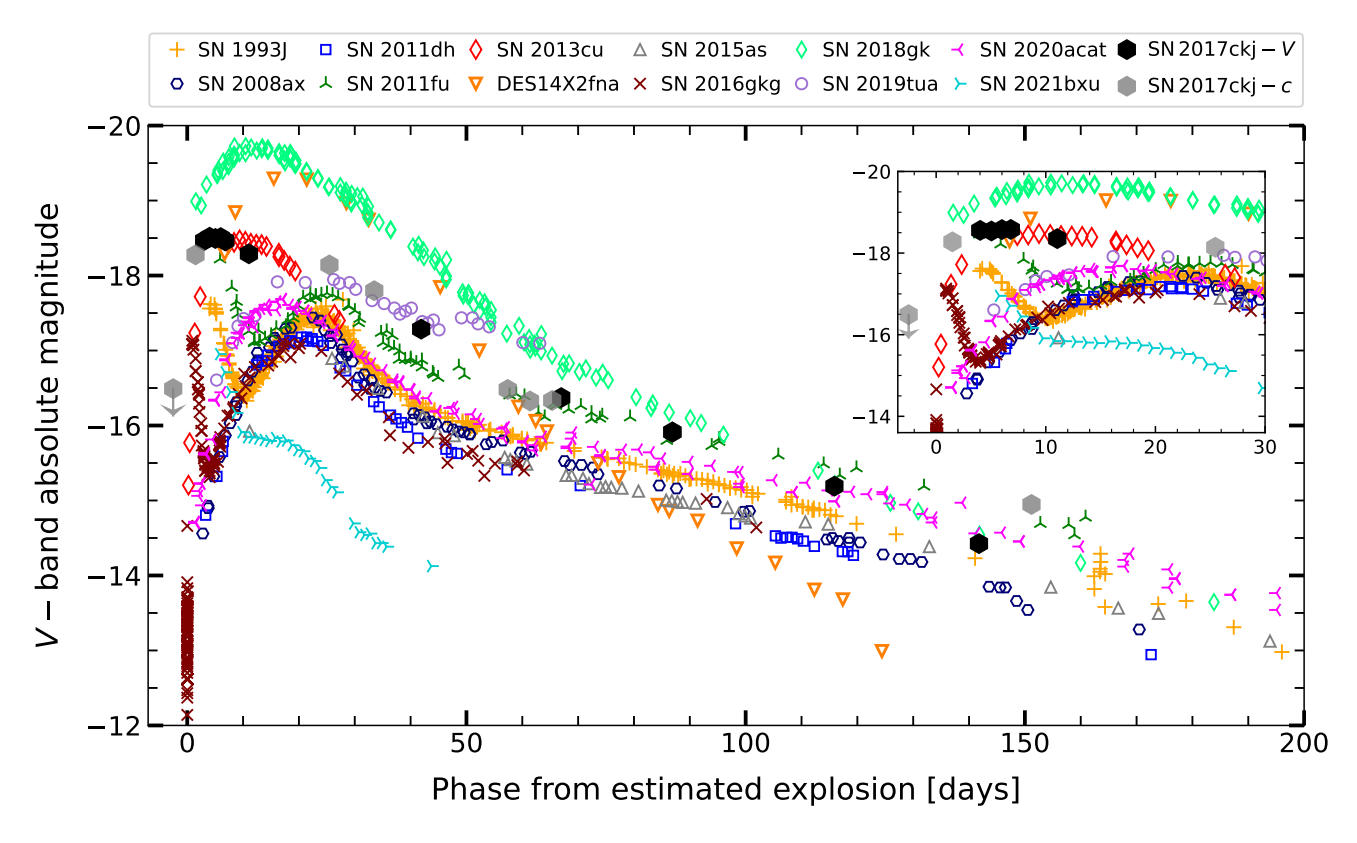


Fig. 3: Absolute V-band light curve of SN 2017ckj compared to other SNe IIb. The ATLAS absolute c-band data of SN 2017ckj are also plotted with grey prismatic dots, as the V-band data is missing from 15 to 40 days. The subplot (upper right) displays the initial 30 days of absolute light curves. Note that DES14X2fna and SN 2013cu lack the V-band observations, therefore, we substitute with r-band data.

We therefore estimated the post-maximum decline rates of SN 2017ckj in different bands by performing a linear regression on the post-peak data, as summarized in Table 2. Due to the noticeable change in the light-curve slope around 40 d in the uBgc-bands, we calculated the decline rates from the peak to 40 d ( $\gamma_{0-40}$ ) and from 40 d to 200 d ( $\gamma_{40-200}$ ) for these bands and the overall decline rates for Vroiz-bands. The bluer light curves decay more rapidly than the redder ones during the early phases. For instance, in the early-time light curve, the u-band shows a high decline rate of  $\sim 10$  mag/100 d, while the z-band exhibits a much slower rate of only  $\sim 1.9$  mag/100 d. The late-time decline rates across different bands are relatively shallow, with values around 2 mag/100 d.

The *r*-band decline rate  $\gamma_{0-200}$  of SN 2017ckj is 2.5 mag/100 d, which approaches the upper limit of the distribution seen in some SNe IIb samples (~ 1.3 – 2.5 mag/100 d; Grayling et al. 2021). Notably, DES14X2fna and SN 2018gk, both luminous SNe IIb, exhibit high *r*-band decline rates of  $4.30 \pm 0.10$  and  $3.03 \pm 0.06$ , respectively, which are significantly higher than those of typical SNe IIb (Grayling et al. 2021). Pessi et al. (2019) calculated the magnitude difference between 40 and 30 d post-explosion ( $\Delta m_{40-30}$ ) and proposed that this value for SNe IIb in *B*-band ranges from ~0.6 to 1.2. For SN 2017ckj,  $\Delta m_{40-30}$  of *B*-band is ~ 0.6 through extrapolation from the decline rate  $\gamma_{0-40}$ , which lies near the lower end of this range.

#### 3.2. Absolute light curves

Taking into account the distance and reddening estimates reported in Section 2, we calculated the V-band peak absolute

magnitude of SN 2017ckj as  $M_V = -18.58 \pm 0.17$  mag. The absolute V-band magnitude light curve of SN 2017ckj was compared to those of SN 1993J (Richmond et al. 1994; Barbon et al. 1995; Richmond et al. 1996), SN 2008ax (Pastorello et al. 2008; Tsvetkov et al. 2009; Taubenberger et al. 2011), SN 2011dh (Tsvetkov et al. 2012; Sahu et al. 2013; Brown et al. 2014), SN 2011fu (Kumar et al. 2013), SN 2013cu (Gal-Yam et al. 2014), DES14X2fna (Grayling et al. 2021), SN 2015as (Gangopadhyay et al. 2018), SN 2016gkg (Arcavi et al. 2017; Bersten et al. 2018), SN 2018gk (Bose et al. 2021), SN 2019tua (Huang et al. 2024), SN 2020acat (Medler et al. 2022), SN 2021bxu (Desai et al. 2023). These SNe IIb were chosen as comparison objects for SN 2017ckj as they all possess comprehensive photometric and spectroscopic data around peak time. The basic properties and information of those SNe IIb are listed in Table C.1 of Appendix C.

In Figure 3, we presented the comparison of the absolute *V*-band magnitudes for a subset of these SNe IIb samples. Note that we additionally plotted the absolute *c*-band data (grey hexagonal dots) of SN 2017ckj to supplement the observational coverage. The *V*-band peak absolute magnitude of SN 2017ckj ( $M_V = -18.58 \pm 0.17$  mag) is brighter than most typical SNe IIb, such as SN 1993J ( $M_V = -17.57 \pm 0.17$  mag; Richmond et al. 1994), SN 2008ax ( $M_V = -17.61 \pm 0.43$  mag; Taubenberger et al. 2011), SN 2011fu ( $M_V = -17.76 \pm 0.15$  mag; Morales-Garoffolo et al. 2015), SN 2015as ( $M_V = -16.82 \pm 0.18$  mag; Gangopadhyay et al. 2018), and SN 2020acat ( $M_V = 17.62 \pm 0.11$  mag; Medler et al. 2022). However, SN 2017ckj is fainter than both DES14X2fna ( $M_V = -19.37 \pm 0.05$  mag; Grayling et al. 2021) and SN 2018gk ( $M_V = -19.70 \pm 0.27$  mag; Bose et al. 2021).

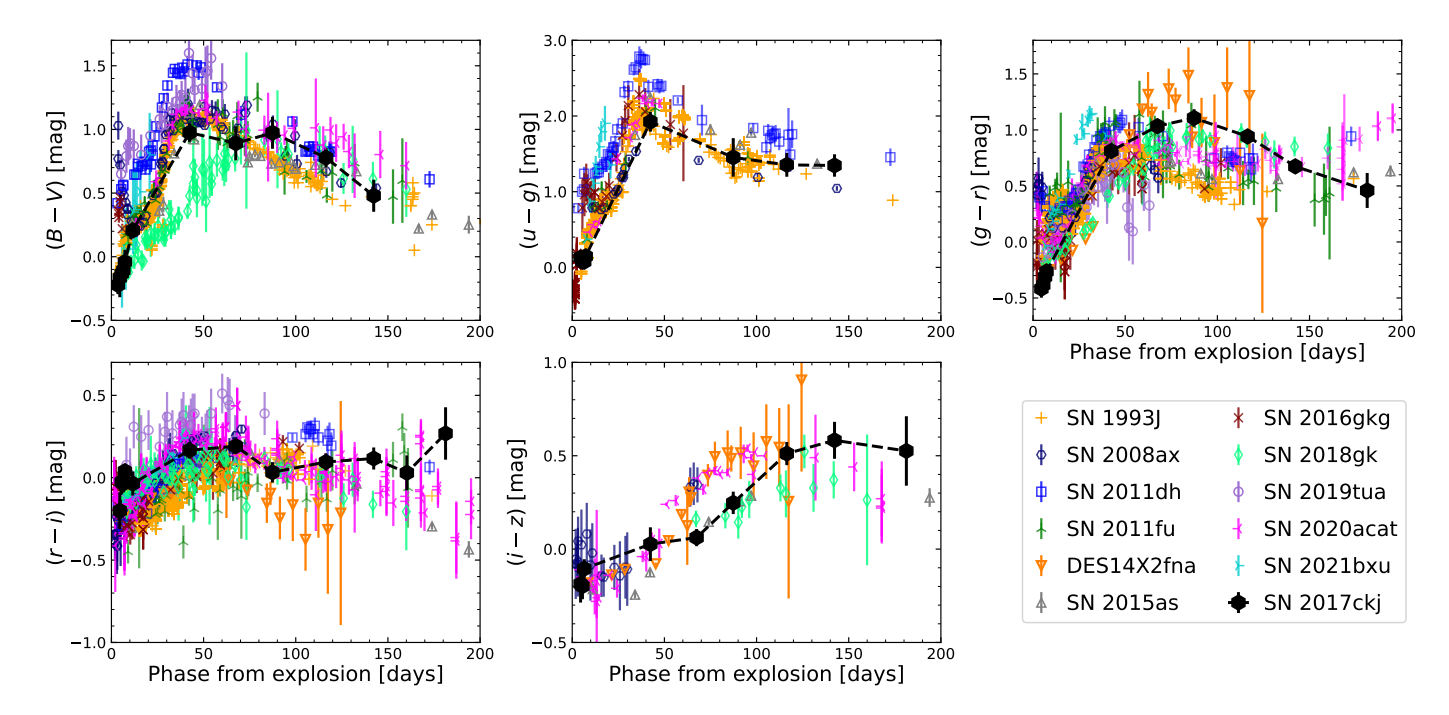


Fig. 4: Colour evolution of SN 2017ckj based on the estimated explosion epoch, compared with those of a sample of SNe IIb. The colour curves are corrected for Galactic and host galaxy extinction.

In the subplot of Figure 3, some typical SNe IIb, such as SN 1993J, SN 2011fu, and SN 2016gkg, exhibit light curve evolution characterized by an initial decline followed by a rise to a peak around 20 d after the estimated explosion epoch. The initial decline observed in these SNe IIb is caused by the shockcooling phase of the thin H-rich envelope, while the subsequent rise phase is powered by radioactive heating from <sup>56</sup>Ni decay (Nakar & Piro 2014). However, not all SNe IIb exhibit evidence of a shock-cooling tail, likely due to their lower envelope masses or more compact progenitor (lower radius). For SN 2017ckj, the light curve peaks earlier and reaches a relatively higher luminosity, distinguishing it from most typical SNe IIb. It is worth noting that the brightness of SN 2017ckj compared to SN 2013cu, DES14X2fna, and SN 2018gk is relatively high for typical SNe IIb, and the trends in their light curves are remarkably similar, particularly for SN 2013cu.

#### 3.3. Colour evolution

For the colour evolution, due to the differences in the observed photometric bands among the SNe IIb samples, additional data were added by using the colour conversion from Jordi et al. (2006), of

$$(u-g) = (0.750 \pm 0.050)(U-B) + (0.770 \pm 0.070)(B-V) + (0.720 \pm 0.040)$$
 (1)

$$(g-r) = (1.646 \pm 0.008)(V-R) - (0.139 \pm 0.004) \tag{2}$$

$$(r-i) = (1.007 \pm 0.005)(R-I) - (0.236 \pm 0.003)$$
 (3)

By applying the extinction correction, the colour evolution of SN 2017ckj and the comparison with those of SNe IIb listed in Table C.1 of Appendix C is shown in Figure 4. Overall, the colour evolution of SN 2017ckj is similar to that of typical SNe IIb. The early colours of SN 2017ckj exhibit a reddening trend, with the B-V colour increasing by  $\sim 1.5$  mag, leading up to the peak at  $\sim 50$  d. This evolution is driven by the cooling of the

expanding ejecta and the corresponding shift of the blackbody emission peak toward longer wavelengths. After the red peaks, colours of B-V, u-g and g-r slowly decline over the next  $\sim 150\,\mathrm{d}$ . This decline is expected as the ejecta becomes optically thin, allowing trapped photons to escape the inner ejecta. However, there is no significant downward trend in the colours of r-i and i-z during 50 to 150 d, which is due to the emergence of the  $[O_1] \lambda\lambda 6300$ , 6364 and  $[Ca_{II}] \lambda\lambda 7292$ , 7324 lines that dominate the spectra at this phase.

It is worth noting that a rapid blueward colour evolution within about the first two weeks could be seen in SN 2008ax and SN 2020acat. The two SNe have been suggested to have a compact progenitor and lack a pronounced shock-cooling tail, which typically manifests as an initially very blue colour that subsequently transitions to red (Medler et al. 2022). In contrast, the early colour evolution of SN 2017ckj does not exhibit a rapid bluing phase in the first two weeks, consistent with the behaviour of most SNe IIb, including SN 1993J. These SNe generally possess a relatively extended H-rich envelope that expands rapidly after the explosion, resulting in a redder colour evolution until about 50 days. This suggests that SN 2017ckj may also have an extended envelope similar to those of typical SNe IIb.

#### 3.4. Pseudo-bolometric light curves

A pseudo-bolometric light curve of SN 2017ckj was constructed by using the photometric *uBgcVroiz*-bands. The fitting procedure for the bolometric light curve employed the publicly accessible Superbol<sup>3</sup> program (Nicholl 2018). Superbol constructs the pseudo-bolometric light curves by integrating extinction-corrected fluxes across observed bands. Taking into account the distance and reddening estimates reported in Section 2, we calculated the pseudo-bolometric light curve of SN 2017ckj and several SNe IIb listed in Table C.1 of Appendix C, as

<sup>3</sup> https://github.com/mnicholl/superbol

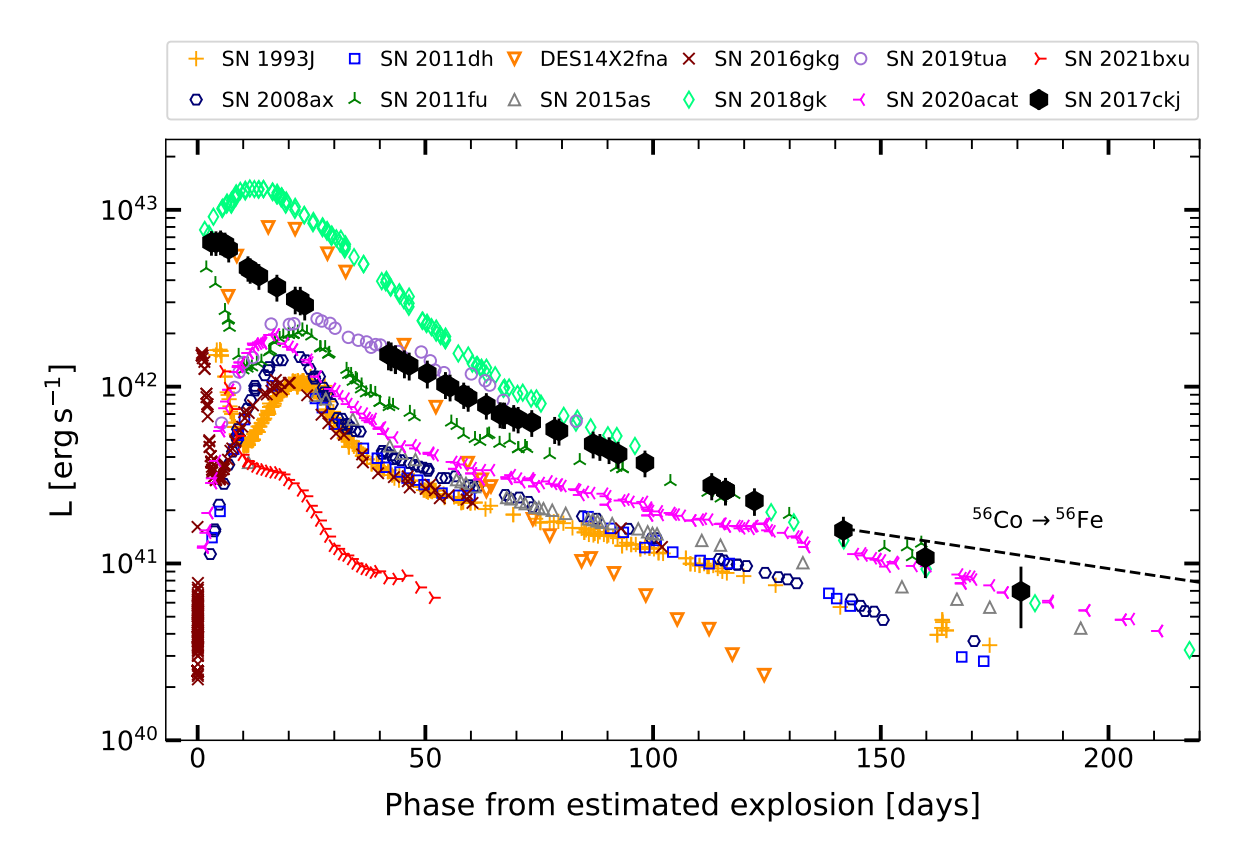


Fig. 5: The pseudo-bolometric light curve of SN 2017ckj, along with several other well-observed SNe IIb over the first 200 d. All SNe have been corrected for reddening as well as time dilation.

shown in Figure 5. To consistently compare luminosities, we constructed pseudo-bolometric light curves for our comparison sample of SNe IIb using the same available photometric bands. If a SN lacked Sloan filters, we used the corresponding Johnson–Cousins filters to cover a similar wavelength range. Note that SN 2019tua lacked the U-band observation, and DES14X2fna had the photometric observation of griz-bands, which did not have a major effect on the comparisons. Also shown in Figure 5 is the theoretical decay slope of  $^{56}$ Co (black dashed line), which is expected to dominate the late-time luminosity evolution of SNe.

The pseudo-bolometric light curve of SN 2017ckj peaks at a luminosity of  $L_{\rm peak}=6.59^{+0.49}_{-0.49}\times10^{42}\,\rm erg\,s^{-1}$ . SN 2017ckj displays a higher peak luminosity than the majority of SNe IIb shown in Figure 5, such as SN 1993J, SN 2015as, and SN 2020acat. Among the SNe of our sample, only SN 2018gk and DES14X2fna have higher peak luminosity than SN 2017ckj. The late-time luminosity evolution of SN 2017ckj resembles that of SN 2011fu, although SN 2017ckj does not exhibit a clear shock-cooling tail as seen in SN 2011fu. This similarity of late-time light curves suggests that a comparable mass of  $^{56}$ Ni was synthesized in the SN explosion.

# 3.5. Bolometric light curve modelling

The late-time evolution of SN 2017ckj exhibits a significantly steeper decline than that expected from the radioactive  $^{56}$ Co decay (see Figure 5), which is likely due to an incomplete trapping of the  $\gamma$ -rays produced in the radioactive decay (Wheeler et al. 2015). A simple relation to describe the late-time photometric evolution by Clocchiatti & Wheeler (1997) for a sample of SE-

SNe is

$$L(t) = L_0(t) \times \left[ 1 - e^{-(T_0/t)^2} \right]$$
 (4)

Here,  $T_0$  the full-trapping characteristic timescale defined as

$$T_0 = \left(C\kappa_\gamma \frac{M_{\rm ej}^2}{E_k}\right)^{1/2} \tag{5}$$

where  $M_{\rm ej}$ ,  $E_k$  and  $\kappa_{\gamma}$  are the total ejected mass, kinetic energy, and the  $\gamma$ -ray opacity. C is a constant given by  $C = (\eta - 3)^2 [8\pi(\eta - 1)(\eta - 5)]$  for a density profile of the radioactive matter  $\rho(r, t) \propto r^{-\eta}(t)$ .

By assuming spherical symmetry and homologous expansion of shells with all radioactive material concentrated at the center, Jerkstrand et al. (2012) provided the theoretical luminosity under the condition of complete trapping of the energy deposited by the decay of <sup>56</sup>Co.

$$L_0(t) = 9.92 \times 10^{41} \frac{M_{\text{Ni}}}{0.07 \,\text{M}_{\odot}} \left( e^{-t/111.4} - e^{-t/8.8} \right) \text{erg s}^{-1}, \tag{6}$$

where  $M_{\rm Ni}$  is the <sup>56</sup>Ni mass expelled by the SN explosion.

Therefore, we fitted the late-time bolometric light curve of SN 2017ckj using MCMC simulations to obtain an estimate of the ejected  $^{56}\rm{Ni}$  mass and the full-trap characteristic timescale. The full bolometric light curve of SN 2017ckj was also constructed using Superbol based on the blackbody assumption. The best fitting  $^{56}\rm{Ni}$  mass is  $0.21^{+0.05}_{-0.03}\,\rm{M}_{\odot}$  and the full-trapping characteristic timescale  $T_0$  is  $84.6^{+0.5}_{-12.1}$  d. The corresponding fitting and MCMC sampling results are presented in Figure A.2 of Appendix A.

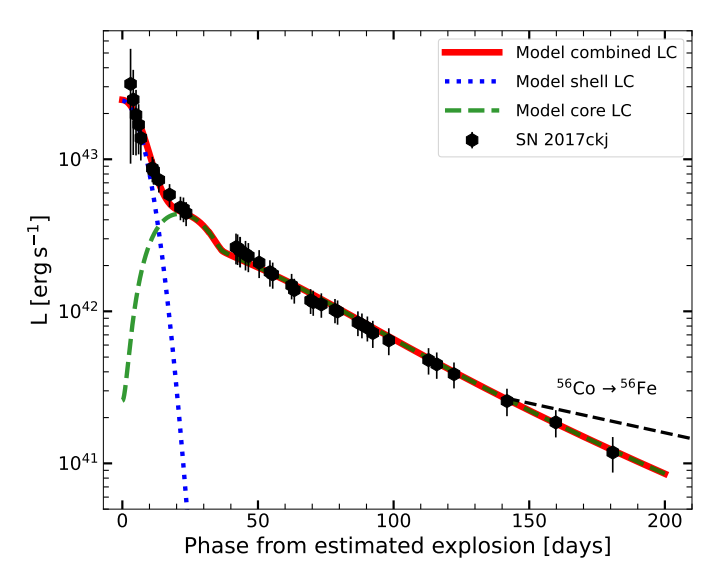


Fig. 6: The full bolometric light curve of SN 2017ckj (black dots) fitted with the two-component model of Nagy & Vinkó (2016), including  $\gamma$ -ray leakage. The green and blue curves represent the contribution from the He-rich core and the extended H-envelope, respectively, while the red line shows the combined light curve.

Table 3: Model parameters of SN 2017ckj

Parameters	Core	Envelope	Remarks
$R_0 (10^{12} \text{ cm})$	0.35	40	Progenitor radius
$M_{\rm ej}~(M_{\odot})$	1.6	0.4	Ejecta mass
$M_{ m Ni}~(M_{\odot})$	0.21	-	Nickel mass
$\kappa$ ( cm <sup>2</sup> /g)	0.2	0.3	Thomson scattering opacity
$E_{\rm tot} \ (10^{51} {\rm erg})$	4.4	5.0	Total energy
$E_{ m kin}/E_{ m th}$	1.75	4.0	The ratio of ejecta kinetic en-
			ergy to thermal energy
$A_g$ (day <sup>2</sup> )	7157	7157	The factor represents the effectiveness of $\gamma$ -ray trapping

Using the mean parameter from MCMC simulations, we applied the two-component light curve model of Nagy & Vinkó (2016) to fit the full bolometric light curve of SN 2017ckj. The model is based on a two-component configuration consisting of a dense inner He-rich region and an extended low-mass H-rich envelope for SNe IIb. The light curve is thus the combination of radiation from the shock-heated ejecta and the radioactive decay of  $^{56}$ Ni to  $^{56}$ Co. Here, we adopted  $\kappa=0.3~{\rm cm^2/g}$  for the outer envelope and  $\kappa=0.2~{\rm cm^2/g}$  for the inner core, which is the same as the setting of Nagy & Vinkó (2016). In practice, we first fitted the core properties based on the previous late-time MCMC fitting results, and then constrained the envelope properties since the strength of the early-cooling emission depends on the underlying  $^{56}$ Ni-heating light curve.

The fitting result of the bolometric light curve is shown in Figure 6, and the best-fit parameters are summarised in Table 3. It is worth noting that  $A_g = T_0^2$ , where  $A_g$  is the factor that represents the effectiveness of  $\gamma$ -ray trapping. In Figure 6, the high early-time blackbody temperature of SN 2017ckj makes SED fitting with optical bands challenging, resulting in large uncertainties in the early luminosity. Given the uncertainties of the early luminosity and the contribution from underlying

Table 4: Model parameters of the comparison SNe IIb.

SNe IIb	$M_{ m shell}$	$M_{ m Ni}$	$M_{\rm core}$	$E_{ m kin}$	References
	$(M_{\odot})$	$(M_{\odot})$	$(M_{\odot})$	$(10^{51}erg)$	
2017ckj	$0.4^{+0.1}_{-0.1}$	$0.21^{+0.05}_{-0.03}$	1.6	2.8	This work
1993J	0.1	0.1	2.15	2.4	1
2008ax	-	0.07-0.15	2-5	1-6	2
2011dh	0.1	0.06	~ 2	0.6-1.0	3
2011fu	0.12	0.23	2.2	2.4	1
2015as	0.1	0.08	1.1-2.2	0.78	4
2020acat	0.1	$0.12 \pm 0.03$	$2.3 \pm 0.4$	$1.2 \pm 0.3$	5, 6
2021bxu	$0.065^{+0.005}_{-0.005}$	$0.029^{+0.004}_{-0.005}$	-	-	7
2022crv	0.015-0.05	0.12±0.05	3.2-3.9	3.4	8

References: 1. Nagy & Vinkó (2016), 2. Taubenberger et al. (2011), 3. Bersten et al. (2012), 4. Gangopadhyay et al. (2018), 5. Medler et al. (2022), 6. Ergon et al. (2024), 7. Desai et al. (2023), 8. Gangopadhyay et al. (2023).

<sup>56</sup>Ni heating, we constrained the mass of the H-rich envelope to  $M_{\rm ej} = 0.4^{+0.1}_{-0.1} M_{\odot}$  to match the observed early high luminosity.

We also summarised the model parameters of other SNe IIb in Table 4. SN 1993J, SN 2011dh, SN 2011fu, and SN 2015as possess relatively massive H-rich envelopes of  $\sim 0.1\,M_\odot$ , whereas SN 2021bxu and SN 2022crv are inferred to have significantly lower mass envelopes, on the order of a few 0.01  $\rm M_\odot$ . To account for the early high luminosity, SN 2017ckj requires a more massive and extended H-rich envelope of  $\sim 0.3-0.5\,M_\odot$  to produce a luminous and long-lasting shock-cooling tail. Although this value exceeds those of SNe IIb in our comparison sample, it still lies within the canonical mass range of SNe IIb  $(0.001-1.0\,M_\odot;$  Yoon et al. 2017).

Additionally, for SN 2017ckj, the high <sup>56</sup>Ni mass is particularly notable, exceeding that of the majority of SNe IIb. Among known cases listed in Table 4, only SN 2011fu exhibits a comparable <sup>56</sup>Ni mass of 0.23  $M_{\odot}$  (Nagy & Vinkó 2016), and its late-time pseudo-bolometric light curve closely resembles that of SN 2017ckj in Figure 5. Prentice et al. (2016) suggested the median <sup>56</sup>Ni mass for SNe IIb is approximately  $0.11^{+0.04}_{-0.04} M_{\odot}$ , whereas SN 2017ckj clearly exceeds this range. The luminous SNe IIb DES14X2fna and SN 2018gk would require <sup>56</sup>Ni masses of  $\sim 0.6$  and  $\sim 0.4 M_{\odot}$ , respectively, under the assumption of a standard <sup>56</sup>Ni decay model (Grayling et al. 2021; Bose et al. 2021). Their exceptionally high luminosities may indicate the need for an additional power source, such as interaction with circumstellar material (CSM) or energy input from a rapidly rotating neutron star (magnetar, Grayling et al. 2021).

# 4. Spectroscopy

# 4.1. Spectral sequence

Figure 7 shows the spectral evolution of SN 2017ckj until the start of the nebular phase. The first spectrum of SN 2017ckj is obtained on 28 March 2017 (MJD = 57840.1), approximately 3.0 d after the estimated explosion date. It exhibits a blue continuum with a blackbody temperature of  $\sim 22\,000\,\mathrm{K}$ , reflecting the high temperature of the ejecta shortly after the explosion. In addition, weak but distinct narrow emission lines of H $\alpha$ , H $\beta$ , and

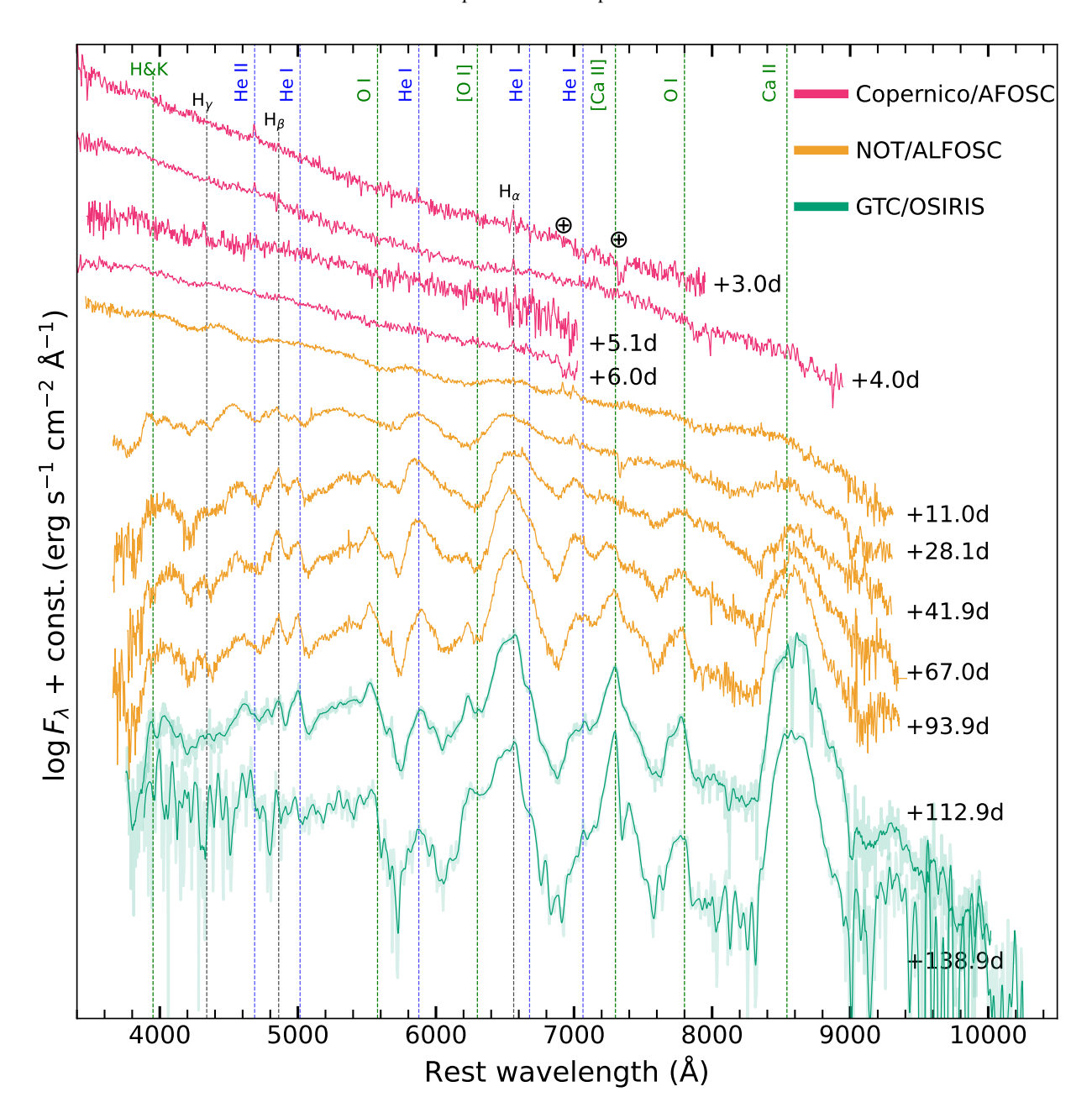


Fig. 7: Spectral sequences of SN 2017ckj. The positions of the principal transitions from H, He and other spectral elements are highlighted by the dashed vertical lines. The  $\oplus$  symbols mark the position of the strongest telluric absorption bands. The phase of spectra based on the estimated explosion epoch (MJD =  $57837.1 \pm 0.1$ ) is given on the right-hand side. All spectra have been corrected for redshift and extinction. The last two spectra, with lower signal-to-noise ratio (S/N), have been smoothed using a Savitzky-Golay filter.

He II  $\lambda$ 4686 are also present at this phase. These flash-ionization features are tentatively identified in the early-time spectra, and are thought to originate from the recombination of CSM that was ionized by the initial shock-breakout radiation pulse, similar to those observed in the early spectra of SN 2018gk (Bose et al. 2021), SN 2013cu (Gal-Yam et al. 2014), and SN 2022lxg (Charalampopoulos et al. 2025). By +6.0 d, the blackbody temperature of the spectrum has cooled significantly, although it still shows a blue continuum, now corresponding to a blackbody temperature of around 10 000 K. At this stage, the He II  $\lambda$ 4686 emission lines have faded, while the H $\alpha$  line remains marginally visible.

At +11.0 d from the explosion, the blue continuum has faded. By +28.1 d, broad P-Cygni profiles are more clearly devel-

oped, indicating an expanding photosphere and the transition into the photospheric phase. Broad P-Cygni profiles of  $H\alpha$ ,  $H\beta$ ,  $H\gamma$ ,  $He_1\lambda\lambda5876$ , 7065, O 1 and Ca II begin to appear and steadily strengthen. The  $He_1\lambda6678$  feature is not clearly detected, which may be due to its intrinsically low flux or significant blending with the prominent  $H\alpha$  emission, making it difficult to distinguish. It is worth noting that the P-Cygni profile of  $H\alpha$  in the +41.9 d spectrum exhibits a notch caused by the overlapping P-Cygni absorption of  $He_1\lambda6678$ . This notch feature is similar to that seen in SN 1993J at +41 d, although it is not as prominent as in SN 1993J (Barbon et al. 1995).

In the blue region of the optical spectrum at this stage, where Fe II features typically dominate, a strong absorption feature

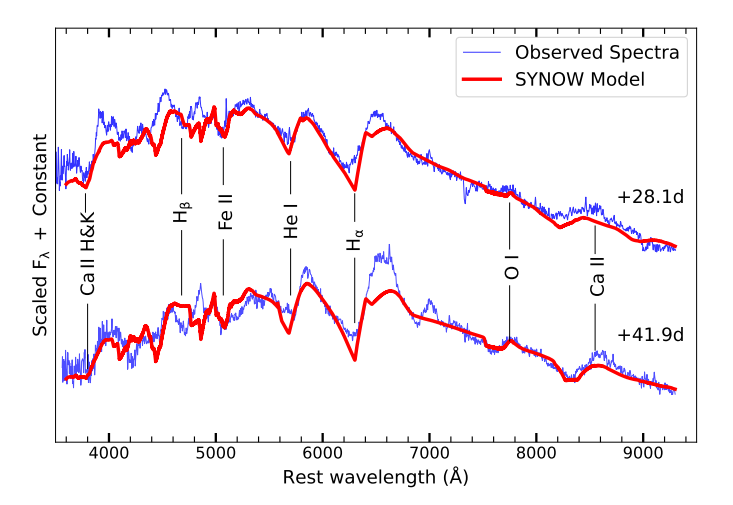


Fig. 8: The SYNOW models and line identifications for SN 2017ckj at two epochs. The observed spectra are corrected for extinction and redshift. All prominent permitted lines are labelled by marking the corresponding component.

appears near 4900Å, comparable in depth to the H $\beta$  feature at +41.9 d after the explosion. This feature is generally attributed to Fe II  $\lambda$ 5018. Notably, the He I  $\lambda$ 5016 could also contribute to the 4900Å feature. However, it is significantly weaker than He I  $\lambda$ 5876, making it unlikely that He I  $\lambda$ 5016 alone is responsible for the observed absorption (Drake 2006). The N II  $\lambda$ 5005 could also contribute to this feature, but its contribution is likely limited due to the relative weakness of N II  $\lambda$ 5680.

As time goes by, forbidden emission lines of [O1]  $\lambda\lambda6300$ , 6364 and  $[Ca\,II]$   $\lambda\lambda7291$ , 7324, which are characteristic nebular-phase features, become prominent from +67.0 d onwards. In the nebular-phase spectra, the intensity of  $H\alpha$  profile does not show a significant weakening trend up to the last available spectrum on +138.9 d, while the [O1]  $\lambda\lambda6300$ , 6364 emission feature gradually strengthens over time. In contrast, for SN 1993J, the  $H\alpha$  emission profile is significantly weaker than [O1] emission in its +139 spectrum (Matheson et al. 2000). This unusually strong  $H\alpha$  emission of SN 2017ckj suggests the presence of a relatively massive hydrogen envelope of its progenitor. The  $O1\lambda7774$  feature appears at +28.1 d and gradually strengthens in the subsequent spectra.

The Ca II NIR  $\lambda\lambda$ 8498, 8542, 8662 triplet exhibits weak emission features as early as +11.0 d, followed by rapid strengthening, ultimately becoming a significant feature in the nebular-phase spectra. In the red region of the late-time spectra, the O I  $\lambda$ 9263 emission feature also becomes more prominent over time, despite the low S/N in that wavelength range.

# 4.2. Flash ionization in the early spectra

In the first observed spectrum at  $+3.0 \,\mathrm{d}$ , the narrow emission line of H $\alpha$  and He II likely originates from the recombination of CSM that was flash-ionized by the initial shock-breakout radiation pulse (see e.g. Niemela et al. 1985; Gal-Yam et al. 2014). The flash-ionized emission-line profiles of H $\alpha$  and He II could be described by a combination of a broad Lorentzian and narrow Gaussian components (e.g. Yaron et al. 2017). However, for SN 2017ckj, the flash-ionized emission components cannot be clearly decomposed due to the limited resolution of the early-time spectra. The full width at half maximum (FWHM) of the

overall H $\alpha$  profile is approximately 700 km s<sup>-1</sup>, while that of the He II profile is about 1100 km s<sup>-1</sup>.

Assuming that the H $\alpha$  emission arises from recombination in CSM photoionized by the shock breakout, we can estimate the progenitor mass-loss rate. For this order-of-magnitude estimate, we neglect the additional complexities introduced by light travel time effects (Kochanek 2019). The H $\alpha$  recombination luminosity of a fully ionized hydrogen wind is given by:

$$L_{\text{H}\alpha} = \frac{\dot{M}^2 \alpha_{\text{H}\alpha} \epsilon_{\text{H}\alpha}}{4\pi v_w^2 m_p^2 R_{\text{in}}},\tag{7}$$

where  $\dot{M}$  is the mass-loss rate,  $\alpha_{\rm H}\alpha$  is the Case B H $\alpha$  recombination coefficient, representing the portion of the total Case B recombination coefficient that ultimately produces a H $\alpha$  photon (Storey & Hummer 1995; Tomasella et al. 2014), and  $\epsilon_{\rm H}\alpha = 1.89 \, {\rm eV}$  is the energy of a H $\alpha$  photon. Here,  $v_w$  denotes the wind velocity,  $m_p$  is the proton mass, and  $R_{\rm in}$  represents the inner edge of the wind.

Bose et al. (2021) provided a simplified equation to estimate the required mass-loss rate:

$$\dot{M} \approx 1.4 \left[ \frac{L_{\text{H}\alpha}}{10^{39} \text{erg s}^{-1}} \cdot \frac{R_{\text{in}}}{10^{14} \text{ cm}} \right]^{1/2} \left[ \frac{v_{\text{w}}}{30 \text{ km s}^{-1}} \right]$$

$$\times 10^{-4} \text{ M}_{\odot} \text{ yr}^{-1}.$$
(8)

For the first spectrum of SN 2017ckj, the  $H\alpha$  luminosity is estimated to be  $1.6 \times 10^{39}\,\mathrm{erg\,s^{-1}}$  based on a Gaussian profile fit to the  $H\alpha$  emission feature. The inner edge of the wind is  $R_{\mathrm{in}} \approx R_* + v_s t \approx 3.0 \times 10^{14}\,\mathrm{cm}$  assuming a stellar radius of  $R_* \sim 575\,R_\odot$  and a shock speed of  $v_s = 10^4\,\mathrm{km\,s^{-1}}$ . We adopted a typical wind velocity of  $v_w = 30\,\mathrm{km\,s^{-1}}$  since the observed FWHM velocity is limited by the spectral resolution. Under these assumptions, we estimated a mass-loss rate of  $3.1\times10^{-4}\,M_\odot\,\mathrm{yr^{-1}}$ , which is similar to the typical mass-loss rates of SNe IIb  $(10^{-5}-10^{-4}\,M_\odot\,\mathrm{yr^{-1}}$ , Smith 2014). The early spectra of SN 2018gk also exhibit flash ionization features, indicating a mass-loss rate of  $2\times10^{-4}\,M_\odot\,\mathrm{yr^{-1}}$  (Bose et al. 2021). For comparison, Maeda et al. (2014) suggested that the progenitor of SN 2011dh had a mass-loss rate of  $3\times10^{-6}\,M_\odot\,\mathrm{yr^{-1}}$  during the final ~1300 years before explosion. The progenitor of SN 2013df exhibited a mass-loss rate of  $5.4\times10^{-5}\,M_\odot\,\mathrm{yr^{-1}}$  (Maeda et al. 2015). Given the relatively high mass-loss rate of SN 2017ckj, its progenitor may have undergone an unstable mass-loss phase before explosion, which could result in asymmetric distribution of the CSM density and inferred mass-loss rate around the SNe (e.g. Fransson et al. 1996; Tsang et al. 2022).

The second spectrum of SN 2017ckj, obtained +4.0 d after the explosion, reveals a narrow  ${\rm H}\alpha$  emission feature with a luminosity of  $L_{\rm H}\alpha=1.5\times 10^{39}~{\rm erg~s^{-1}}$ , from which we infer a mass-loss rate of  $3.4\times 10^{-4}~M_{\odot}~{\rm yr^{-1}}$ . The third spectrum could not be analyzed due to insufficient S/N. The fourth spectrum, taken at +6.0 d, similarly displays a narrow  ${\rm H}\alpha$  feature with a luminosity of  $L_{\rm H}\alpha=2.0\times 10^{39}~{\rm erg~s^{-1}}$ , indicating a mass-loss rate of  $4.7\times 10^{-4}~M_{\odot}~{\rm yr^{-1}}$ . Notably, the increase in the inferred mass-loss rate may be due either to a larger amount of CSM being excited by the shock or to the wind being further excited by photons from the ongoing circumstellar interaction. Furthermore, a substantial fraction of the  ${\rm H}\alpha$  narrow emission may originate from collisional excitation rather than recombination (Fransson et al. 1996). The model assumptions carry uncertainties, as we adopted a simplified prescription applied uniformly across different phases.

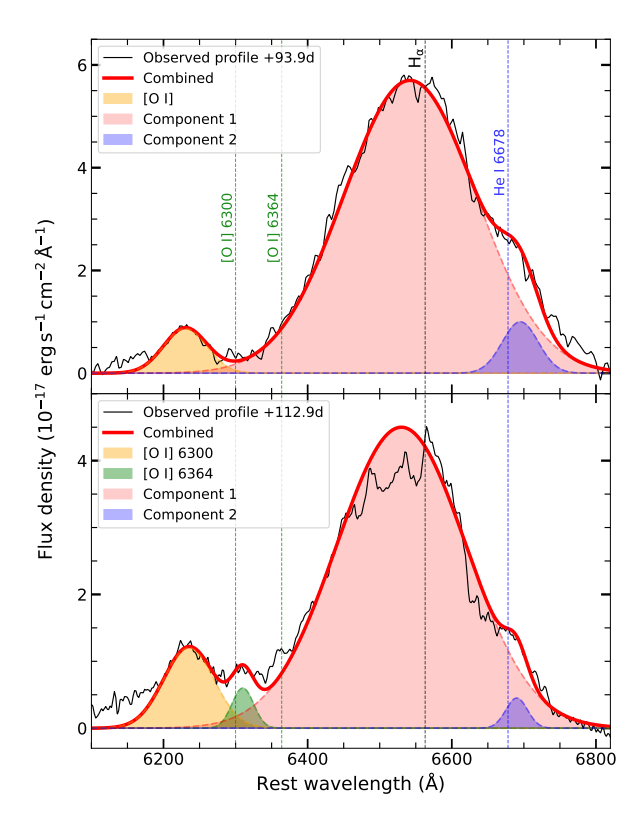


Fig. 9: Decomposition of the emission profile around 6100-6800 Å in the +93.9 d and +112.9 d spectra. The vertical dashed lines show the rest wavelengths of the [O  $_{\rm I}$ ] doublet, H $_{\rm C}$  and He  $_{\rm I}$ .

# 4.3. Line identifications

We modelled the spectra by adopting SYNOW (Fisher et al. 1997; Branch et al. 2002) and identified the spectral lines using a set of atomic species:  $H\alpha$ ,  $He_{I}$ ,  $O_{I}$ ,  $Fe_{II}$ ,  $Ti_{II}$ ,  $Sc_{II}$ ,  $Ca_{II}$ , and Ba II. The models with the line identifications at two phases are shown in Figure 8. The SYNOW code is based on several simplifying assumptions: spherical symmetry, homologous expansion, and the presence of a sharp photosphere that emits a blackbody continuum and is associated with a shock front at early times. It is worth noting that SYNOW is suitable only for modelling spectra during the photospheric phase. SYNOW is designed to model permitted resonance lines formed via resonant scattering in rapidly expanding ejecta, and does not account for the low-density conditions that produce forbidden emission. In our analysis, we modelled the +28.1 and 41.9 d spectra and primarily focused on the absorption components of P-Cygni profiles, which offer insights into the expansion velocities of different line-forming layers, see Figure 8. Although the SYNOW model does not fully reproduce these profiles, particularly on the blue side of the spectrum ( $\lambda < 5500\text{Å}$ ), the dominant line species are identified, such as  $H\alpha$ ,  $He_{I}$ ,  $O_{I}$ ,  $Ca_{II}$ , and  $Fe_{II}$ .

Additionally, the late-time spectra of SN 2017ckj exhibit the prominent emission profile around  $H\alpha$  line. We therefore made the decomposition of the emission profile around 6100-6800Å in the late-time spectra, as shown in Figure 9. The spectrum at +138.9 d is not modelled due to its low S/N. In the top panel, we used three Gaussian components to fit the full emission profile at +93.9 d, including a blueshifted [O I], a broad and strong component 1, and a weak component 2. The [O I]  $\lambda$ 6300 profile is identifiable, whereas the  $\lambda$ 6364 component ap-

pears to be weak or absent. As a result, the [O I]  $\lambda6364$  line was not included in the spectral fit at this phase. Component 1 appears to be a distinct and broad H $\alpha$  emission line, although it may represent a blended profile that includes contributions from C II  $\lambda\lambda6578,6583$ , Si II  $\lambda\lambda6347,6371$  and [N II]  $\lambda\lambda6548,6583$ . Component 2, which is relatively weak, could be attributed to a redshifted He I emission feature.

In the bottom panel of Figure 9, the full emission profile at +112.9 d is modelled using four Gaussian components. Two of these represent the blueshifted [O1]  $\lambda\lambda6300$ , 6364 doublet, while the remaining two components account for additional blended flux. At this stage, the [O1] doublet grows, with the  $\lambda6364$  component appearing relatively distinct. The flux of Component 1 shows a gradual decrease. Component 2 seems to exhibit a blueshifted absorption feature around 6650 Å. Notably, both spectra display a noticeable bump on the blue side near the [O1] profile. This feature, compared with the fitting results, indicates the presence of an underlying broad emission component.

### 4.4. Comparison of Type IIb SN spectra

Figure 10 compares the early-, intermediate-, and late-time spectra of SN 2017ckj with those of other SNe IIb, including SN 1993J, SN 2011fu, SN 2013cu, SN 2016gkg, SN 2018gk, and SN 2020acat. In panel (A), we illustrate the earliest spectra of SN 2017ckj on +3.0 d with those of other SNe IIb at similar phases. These early spectra exhibit a blue continuum, indicating a high blackbody temperature shortly after the explosion. In addition, they display prominent emission features of H $\alpha$  and He II  $\lambda$ 4686. Notably, the early spectra of SN 2017ckj likely exhibit a He I  $\lambda$ 5876 emission feature, which is absent in other SNe IIb.

The spectrum of SN 2017ckj at  $\sim$ 30 d post-explosion is also compared to the other SNe IIb at similar epochs, as shown in panel (B) of Figure 10. Although the  $H\alpha$  P-Cygni features are present in all spectra at this phase, their strength and width vary significantly among different SNe IIb. For SN 2017ckj, the H $\alpha$  feature is quite broad, with a FWHM velocity of  $\sim 12000 \, \mathrm{km \, s^{-1}}$ , comparable to those of SN 2018gk and SN 2011fu. The broad He i P-Cygni features in these SNe IIb exhibit noticeable blueshifts. The central absorption feature within the H $\alpha$  emission profile of SN 2016gkg and SN 2020acat is clearly visible and can be attributed to the P-Cygni absorption of the He I  $\lambda$ 6678 line, whereas this feature is absent in SN 2017ckj and SN 2018gk. All spectra also show Ca II NIR P-Cygni features, although those in SN 2017ckj and SN 2018gk are relatively weak at this stage. Overall, the spectrum of SN 2017ckj at this stage closely resembles that of SN 2018gk.

In panel (C) of Figure 10, the early nebular spectrum of SN 2017ckj at +138.9 d is compared with a subset of SNe IIb. At this phase, all the spectra are dominated by the prominent emission features of [O<sub>1</sub>]  $\lambda\lambda$ 6300, 6364, [Ca II]  $\lambda\lambda$ 7291, 7324, and Ca II NIR  $\lambda\lambda$ 8498, 8542, 8662. Additionally, other metal lines are present, including Mg I]  $\lambda$ 4571, Fe II  $\lambda\lambda$ 4924, 5018, 5169 and O I  $\lambda\lambda$ 77772, 7774. It is worth noting that the spectral features in the range of 6000 – 6800 Å for SN 2017ckj at +138.9 d differ from those of other SNe IIb. At this phase, SNe such as SN 1993J and SN 2011fu exhibit a strong [O<sub>1</sub>]  $\lambda\lambda$ 6300, 6364 emission profile, along with a distinct notch caused by blue-shifted H $\alpha$  and He I lines. However, in SN 2017ckj, the H $\alpha$  and He I lines are blended and cannot be separated into two distinct components. In addition, the Ca II NIR  $\lambda\lambda$ 8498, 8542, 8662 in SN 2017ckj appears to be blended, similar to those in SN 2011fu, SN 2016gkg,

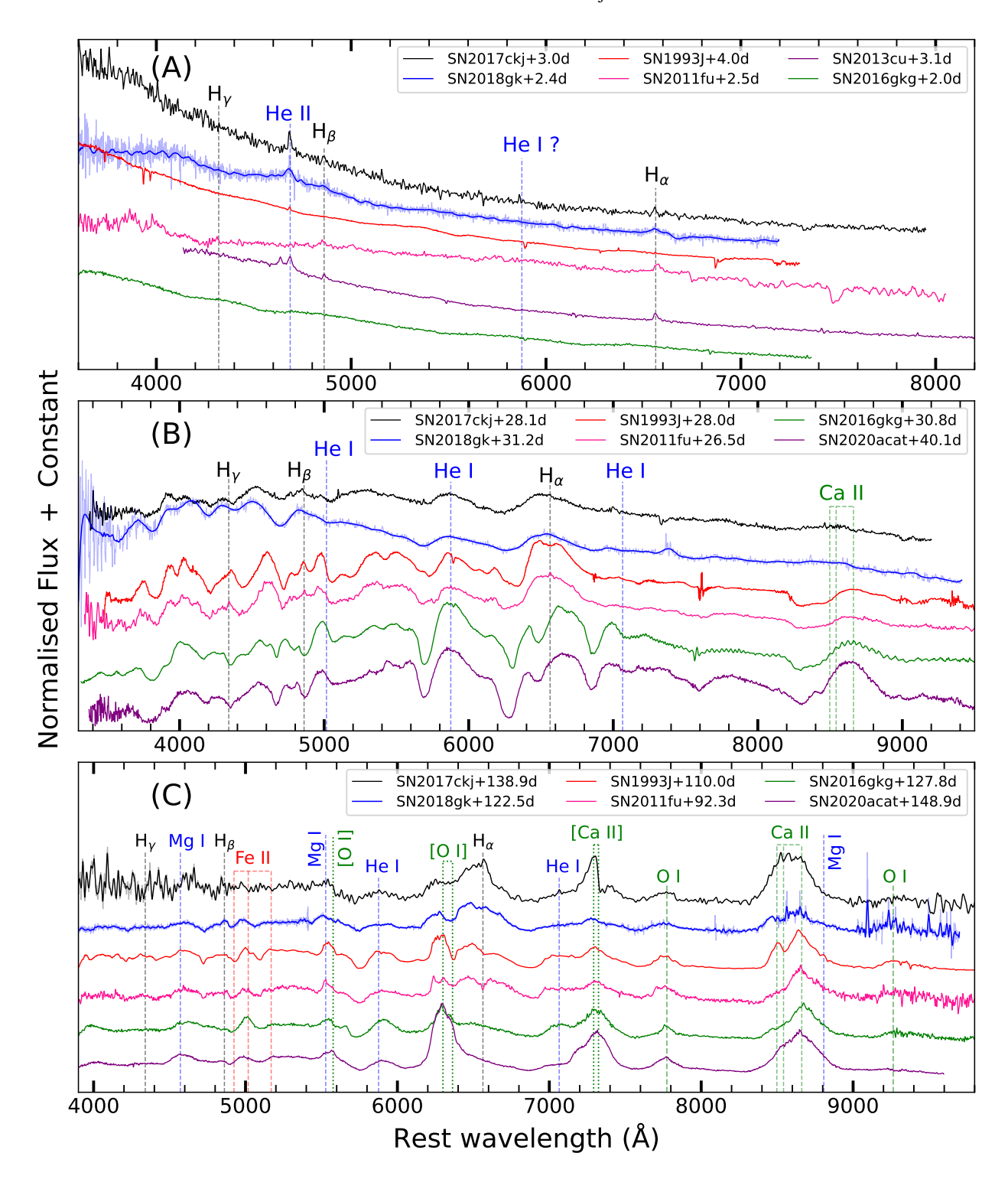


Fig. 10: Early-, intermediate-, and late-time spectroscopic comparisons of SNe IIb. Phase from the explosion date is given in the legend and all spectra are shown in the rest frame. All spectra have been corrected for redshift and extinction. The key line features are marked, with allowed transitions indicated by dashed lines and forbidden lines represented by dotted lines. Some spectra with lower S/N have been smoothed using a Savitzky-Golay filter.

and SN 2020acat. This contrasts with SN 2018gk and SN 1993J, where these emission features can be clearly resolved into multiple components. The observed blending profile may originate from an aspherical explosion geometry, as suggested by Mazzali et al. (2005).

#### 4.5. Spectra line profile and velocity evolution

The evolution of the profiles of the H $\alpha$ , HeI, CaIINIR, and OI peaks in the spectra of SN 2017ckj are shown in Figure 11. The early spectrum at +3.0 d exhibits narrow flash-ionized H $\alpha$  and HeI emission lines. The spectrum at +28.1 d displays distinct P-Cygni profiles, including H $\alpha$ , HeI, CaII and OI, with

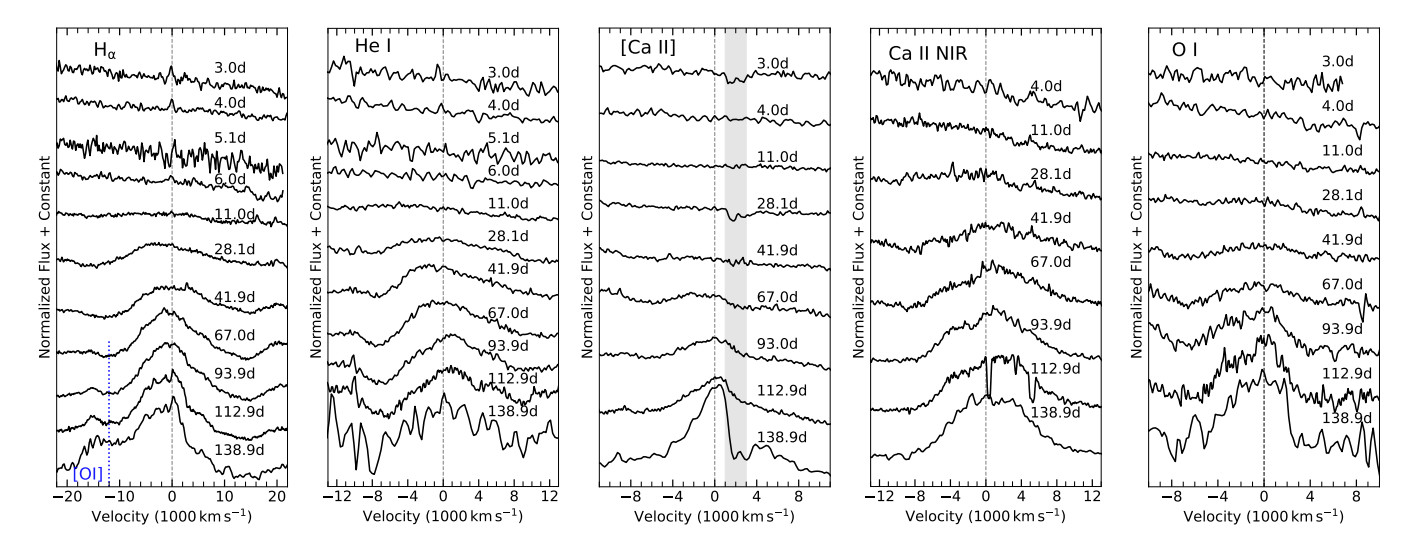


Fig. 11: Line profiles of  $H\alpha$ ,  $He_{I}$ ,  $[Ca_{II}]$ ,  $Ca_{II}$  NIR and  $O_{I}$  within the spectra of SN 2017ckj. The dashed lines represent the emission velocities corresponding to 6563, 5876, 7291, 8571, and 7774 Å lines. The epoch of each spectrum is given in the rest frame, relative to the estimated explosion date.

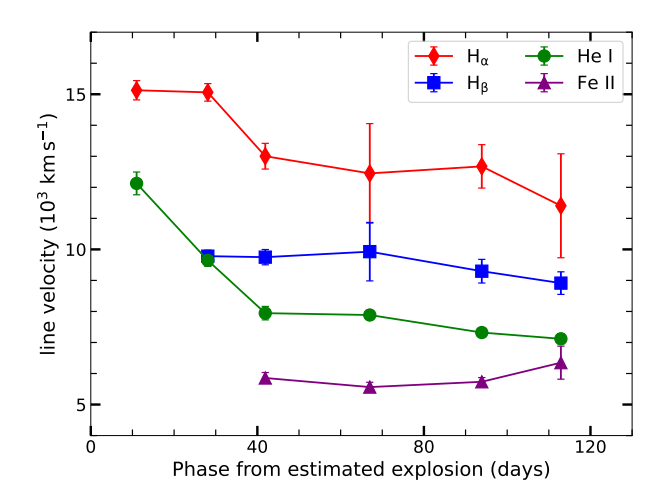


Fig. 12: The line velocity evolution of H $\alpha$ , H $_{\beta}$ , He I  $\lambda$  5876, and Fe II  $\lambda$  5018 for SN 2017ckj, derived from the troughs of their P-Cygni profiles.

significantly higher velocities, indicating a rapidly expanding envelope.

In the panel showing the H\$\alpha\$ profile (Figure 11, left), the blue dotted line indicates the position corresponding to [O\_1] \$\lambda 6300\$ in the H\$\alpha\$ velocity coordinate. The late-time spectrum at +93.9 d shows a weak [O\_1] \$\lambda \lambda 6300\$, 6364 emission profile which gradually strengthens. In the nebular spectra of SNe IIb, the [O\_1] emission profile gradually strengthens over time and becomes prominent at late phases, as seen in the late-time spectrum of SN 2020acat and SN 2016gkg in Figure 10. This is driven by radioactive decay energy deposited in the oxygen-rich core, now revealed by the receding photosphere, allowing forbidden line emissions to emerge in the low-density and expanding ejecta.

At late times, the [Ca  $\pi$ ]  $\lambda\lambda$ 7291, 7324 lines exhibit a notable asymmetry, while the Ca  $\pi$  NIR triplet remains largely symmetric. It is worth noting that distinct absorption features (grey region) appear on the red side of the [Ca  $\pi$ ] emission profile, particularly in the spectra obtained at +3.0, +28.1, and +138.9 days. These absorption features are likely the result of dust extinction,

which contributes to the asymmetric structure observed in the  $[Ca\pi]$  emission in the latest spectrum. Recently, Dessart et al. (2025) proposed that strong forbidden lines in noninteracting SNe II, such as  $[O\tau]$  and  $[Ca\pi]$ , are significantly influenced by dust located within velocities of  $<2000\,\mathrm{km\,s^{-1}}$ . Additionally, the  $O\tau\lambda7774$  profile of the last spectrum appears to exhibit a boxy feature, deviating from the Gaussian-like profile observed at earlier phases, although the spectrum has low S/N. Meanwhile, the peak of  $H\alpha$  profile shows a similar but weaker flattening feature. This  $O\tau$  and  $H\alpha$  flat-topped profile may result from dust absorption on the red side of the emissions or CSM interaction.

The velocity evolution of spectral lines, including  ${\rm H}\alpha$ ,  ${\rm H}\beta$ ,  ${\rm He}\ {\rm I}\ \lambda5876$ , and  ${\rm Fe}\ {\rm II}\ \lambda5018$ , is shown in Figure 12. The line velocities are determined from the absorption minima of P-Cygni profiles, using MCMC-based fitting with a two-component Gaussian profile. The early spectra exhibit a blue continuum, while broad P-Cygni profiles begin to emerge from +11.0 d. The early  ${\rm H}\alpha$  and  ${\rm He}\ {\rm Ie}$  exhibit high expansion velocities of approximately 15000 km s<sup>-1</sup> and 12000 km s<sup>-1</sup>, respectively. Over the first epoch to +41.9 d, the  ${\rm H}\alpha$  and  ${\rm He}\ {\rm Ie}$  velocities decline rapidly. From +41.9 d to +112.9 d, the  ${\rm H}\alpha$ ,  ${\rm H}\beta$ ,  ${\rm He}\ {\rm I}$ , and  ${\rm Fe}\ {\rm II}$  velocities show an approximately constant plateau. At this stage, the velocities of  ${\rm H}\alpha$  and  ${\rm H}\beta$  remain nearly constant at ~ 13000 km s<sup>-1</sup> and ~ 10000 km s<sup>-1</sup>, respectively. In contrast,  ${\rm He}\ {\rm Ie}\ {\rm Ie}\ {\rm Ie}\ {\rm Ie}\ {\rm Ie}\ {\rm Im}\ {\rm Ie}\ {\rm Ie$ 

Overall, the line velocities of absorption features identified in SN 2017ckj are consistent with those of typical SNe IIb (see Medler et al. 2022). The absorption velocity of  $H\alpha$  (12500  $\pm$  800 km s $^{-1}$ ), derived from the weighted measurements of a sample of SNe IIb by Liu et al. (2016), matches well with SN 2017ckj. Similarly, its He  $_{\rm I}$  velocity agrees with the weighted mean of SE-SNe samples (8000  $\pm$  500 km s $^{-1}$ , Fremling et al. 2018). In contrast, the Fe  $_{\rm II}$  velocity in SN 2017ckj is notably lower than most SNe IIb (8400  $\pm$  1400 km s $^{-1}$ , Liu et al. 2016), but comparable to SN 1993J ( $\sim$  6000 km s $^{-1}$ ) and SN 2021bxu ( $\sim$  5000 km s $^{-1}$ ). On the other hand, the velocities of  $H\alpha$  and  $H\beta$  are higher than those of He I, which in turn are higher than those of Fe II. This trend is consistent with the expected layered structure of the progenitor star, where heavier elements are concentrated closer to the core with lower velocities.

#### 5. Discussion

#### 5.1. The nature of light curve evolution

A prominent shock-cooling tail is observed in many SNe IIb, including SN 1993J (Richmond et al. 1994), SN 2011fu (Morales-Garoffolo et al. 2015), SN 2016gkg (Bersten et al. 2018), SN 2024uwq (Subrayan et al. 2025), and SN 2024aecx (Zou et al. 2025). This early-time shock-cooling phase arises from the rapid cooling of the outer stellar layers after the shock breakout at the surface. However, there are some SNe IIb that do not show two distinct peaks and shock-cooling tail, such as SN 2008ax (Pastorello et al. 2008), SN 2020acat (Medler et al. 2022), SN 2022crv (Gangopadhyay et al. 2023), and SN 2024abfo (Reguitti et al. 2025). The absence of an initial long-duration shock breakout cooling peak and distinct shock-cooling tail implies that the progenitor was relatively compact, typically lacking an extended hydrogen envelope. In the light curves of SN 2017ckj, there is a short interval between the initial multi-band observation and the last non-detection limit in c-band. Due to the scarcity of data in this early phase, the possibility of a fastevolving shock-cooling peak occurring during this interval cannot be ruled out.

The majority of SNe IIb that exhibit a distinct shock-cooling tail are believed to originate from progenitors with an extended hydrogen envelope of approximately  $0.1M_{\odot}$  (e.g. Nagy & Vinkó 2016). In contrast, those lacking a clear shock-cooling tail are thought to arise from more compact progenitors with thinner hydrogen envelopes, typically less than  $0.1M_{\odot}$ . For example, SN 2008ax does not exhibit a shock-cooling tail, and its  $H\alpha$  feature disappears by ~50 days after the explosion. Therefore, it was suggested that its progenitor possesses a hydrogen envelope of approximately several times  $0.01M_{\odot}$  (Chornock et al. 2011). Similarly, SN 2022crv was considered to have a  $0.05\,M_{\odot}$  hydrogen envelope, placing it as a continuum between Type Ib and Type IIb SNe (Gangopadhyay et al. 2023; Dong et al. 2024). The  $H\alpha$  feature of SN 2022crv disappears around 35 days after the explosion.

A subset of SNe IIb with peculiar light curve evolution has been identified, including SN 2018gk, DES14X2fna, and SN 2017ckj. As shown in Figure 3, these three SNe IIb exhibit higher peak magnitudes compared to the majority of SNe IIb ( $\sim 1-2$  mag in the V-band). Their light curve evolution deviates from that of typical SNe IIb, including both those with and without an early shock-cooling tail. Under the assumption of a standard <sup>56</sup>Ni decay model, DES14X2fna and SN 2018gk require unusually large <sup>56</sup>Ni masses of ~0.6 and ~0.4  $M_{\odot}$ , respectively (Grayling et al. 2021; Bose et al. 2021). Such high luminosities may suggest the presence of an additional power source, such as interaction with CSM or energy input from a rapidly rotating magnetar (Grayling et al. 2021). Additionally, SN 2022lxg appears to be a SE transitional object, exhibiting early-time spectra similar to those of SNe IIb, while later resembling an interacting Type II supernova (Charalampopoulos et al. 2025). Its light curve evolution is comparable to that of SN 2017ckj, characterized by a luminous peak ( $M_g = -19.41 \text{ mag}$ ) and a short rise time of  $\leq 10$  days. Notably, the early-time g- and r-band light curves of SN 2022lxg exhibit bumps likely caused by CSM interaction, and the late spectral features were suppressed because of CSM interaction after ~35 days. Charalampopoulos et al. (2025) suggested that the interaction between the ejecta and the CSM might contribute to the early-time luminous peak of SN 2022lxg and potentially blend the two components of the SNe IIb light curve.

For SN 2017ckj, a  $^{56}$ Ni mass of  $\sim 0.21 \, \mathrm{M}_{\odot}$  is required to explain its late-time bolometric luminosity evolution. This value is not particularly large compared to those of DES14X2fna and SN 2018gk. The early spectra exhibit the flash ionization features, similar to SN 2018gk. In comparison with typical SNe IIb, SN 2017ckj exhibits a long-lasting and prominent H $\alpha$  emission profile, which persists up to the last available spectrum at +138.9 d. By contrast, other SNe IIb generally do not show such a distinct H $\alpha$  emission feature at similarly late phases. Combining these observational characteristics, we therefore suggested that the peculiar light curve of SN 2017ckj may result from the following scenarios: (1) A progenitor with a relatively massive and extended H-rich envelope (i.e. the outer layers were not significantly stripped) gives rise to a long-lasting shock-cooling phase after the explosion that overlaps and blends with the subsequent <sup>56</sup>Ni-powered peak. This result of overlap leads to a relatively rapid rise in the light curve. This scenario is consistent with the bolometric light curve modelling results shown in Figure 6; (2) A rapidly evolving shock-cooling peak has occurred before the earliest multi-band observations, though it is not seen in the previous ATLAS survey. The subsequent luminous and fast peak could result from a combination of CSM interaction and  $^{56}$ Ni decay. The shock-cooling tail of SNe IIb typically lasts for approximately 1-10 days, depending on the properties of the envelope and the degree of  $^{56}$ Ni mixing. For SN 2016gkg, the shock-cooling tail persists for about 4 days in the V-band (Tartaglia et al. 2017), whereas for SN 2011fu it lasts roughly 10 days (Morales-Garoffolo et al. 2015). Due to the photometric limits of the ATLAS survey and the ~4 days interval between the last non-detection and the first detection, we cannot rule out the presence of a faint, rapidly evolving shock-cooling phase prior to the earliest multi-band observations. This scenario is consistent with the presence of CSM, as indicated by the flash ionization features observed in the early-time spectra. Additionally, the CSM interaction may suppress the emergence of other spectral features, as observed in SN 2022lxg, whose spectrum around 80 d is dominated by H $\alpha$  and Ca II lines, with most other features being notably weak or absent. In contrast, the late-time spectrum of SN 2017ckj at +138.9 d exhibits more prominent spectral features, which may suggest the presence of a relatively thin CSM shell that was rapidly overtaken by the ejecta and thus influenced only the early-time spectra. Further late-time, high-quality spectroscopy and multi-wavelength observations are required to better constrain the nature and extent of the CSM interaction.

# 5.2. The progenitor parameters of SN 2017ckj

In Section 3.5, we proposed a progenitor model for SN 2017ckj consisting of a massive H-rich envelope of  $\sim~0.4\,M_{\odot}$  and an extended envelope radius of  $\sim 575 R_{\odot}$  by adopting the twocomponent model of Nagy & Vinkó (2016). Ouchi & Maeda (2017) calculated a grid of binary evolution models for SNe IIb and provided a sequence to explore the progenitor properties of SNe IIb. Figure 13 shows the relations between stellar radius and H-rich envelope mass, derived numerically from evolutionary models (blue points) and analytically assuming a radiative envelope (black line) under dynamical and thermal equilibrium. To compare with their results, we over-plotted the derived envelope parameters for SN 2017ckj (red star). The envelope parameters of SN 2017ckj are consistent with the relation inferred from hydrodynamical simulations, despite the uncertainty in the envelope mass. Note that the discrepancy between the two approaches becomes more pronounced as the envelope

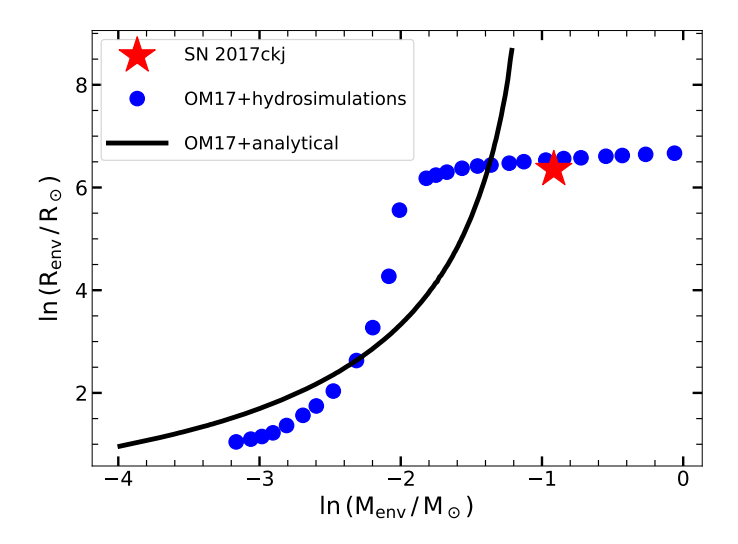


Fig. 13: The relation between the radius and mass of the envelope for the SNe IIb progenitor models (blue dots) from Ouchi & Maeda (2017). The black line represents the analytical relation derived by Ouchi & Maeda (2017), which captures the properties of the numerical evolution models. The parameters derived for SN 2017ckj are indicated by the red star. This figure is modified from Gangopadhyay et al. (2023).

mass increases and convection becomes more significant (Ouchi & Maeda 2017).

We constructed the bolometric luminosity and derived a high  $^{56}\text{Ni}$  mass of  $0.21^{+0.05}_{-0.03}\,M_{\odot}.$  Notably, SN 2011fu exhibits a comparable late-time bolometric luminosity evolution to SN 2017ckj, with an estimated  $^{56}$ Ni mass of 0.23  $M_{\odot}$  (Nagy & Vinkó 2016). Kumar et al. (2013) also fitted the light curve of SN 2011fu with the analytic model of Arnett & Fu (1989) and suggested a <sup>56</sup>Ni mass of 0.21 M<sub>☉</sub>. Therefore, a <sup>56</sup>Ni mass of  $0.22\,\mathrm{M}_\odot$  is plausible for SN 2017ckj, although both SN 2017ckj and SN 2011fu show higher <sup>56</sup>Ni masses compared to typical SNe IIb  $(0.11^{+0.04}_{-0.04} M_{\odot})$ , Prentice et al. 2016). Recent studies have reported two luminous SNe IIb, SN 2018gk and DES14X2fna, with high <sup>56</sup>Ni mass of  $\sim 0.6$  and  $0.4 M_{\odot}$ , respectively, based on the assumption of the standard <sup>56</sup>Ni decay model (Grayling et al. 2021; Bose et al. 2021). However, some studies suggested that the <sup>56</sup>Ni yield in typical CCSNe cannot be too high ( $\sim 0.2 M_{\odot}$ ; Drout et al. 2011; Ertl et al. 2020). Temaj et al. (2024) considered that convective-core overshooting plays an important role in element production (especially <sup>56</sup>Ni) during the final evolutionary stages of massive stars. With an appropriate overshooting prescription, they were able to account for <sup>56</sup>Ni mass yields of up to  $0.26 M_{\odot}$ . However, for overluminous SNe IIb events, such as SN 2018gk and DES14X2fna, additional energy sources beyond radioactive decay are likely required.

Fransson & Chevalier (1989) proposed that the flux ratio of the [Ca II]  $\lambda\lambda$ 7291, 7324 to the [O I]  $\lambda\lambda$ 6300, 6364 emission lines provides a useful diagnostic for estimating the progenitor mass on the main-sequence stage. The [O I]  $\lambda\lambda$ 6300, 6364 emission could trace the oxygen mass synthesized in the core, which reflects the progenitor's initial mass, whereas the calcium emission primarily originates from explosive nucleosynthesis and is thus largely independent of the progenitor's initial mass (e.g. Woosley & Weaver 1995; Thielemann et al. 1996). Fransson & Chevalier (1987, 1989) suggested that the forbidden emission line ratio [Ca II]/[O I] is expected to show an almost constant value at late epochs. Elmhamdi et al. (2004) examined the late-

time evolution of the ratio and showed that the ratio with that of a sample of SNe Ib/Ic is stable after ~250 days of the explosion, consistent with theoretical expectations. Additionally, Jerkstrand et al. (2014) provided the late-time observed luminosity evolution of [O<sub>I</sub>], Mg<sub>I</sub>] and Na<sub>I</sub>D with different initial progenitor masses, which can be used to constrain the oxygen mass. For SN 2017ckj, the last spectrum was obtained at +138.9 d after the explosion. A distinct and strong [O1] emission feature was not observed in the last spectrum, and the prominent H $\alpha$ -like emission makes it difficult to measure flux accurately. In addition, the [Ca II] emission profile appears to be affected by dust absorption. To obtain a rough estimate, the forbidden emission line ratio [Ca II]/[O I] is  $\sim$ 1.4, suggesting that the progenitor of SN 2017ckj has an initial mass of  $\sim 15-17 \, \mathrm{M}_{\odot}$  (Jerkstrand et al. 2014; Ferrari et al. 2024). Notably, the measurements of both [Ca II] and [O I] have large uncertainties, and this result should be treated with caution.

# 6. Concluding remarks

We presented the discovery and follow-up observations of the luminous SN 2017ckj, a fast-rising SN IIb with a V-band rise time of  $\sim 5.0$  d, which is shorter than that of typical SNe IIb. Its absolute peak magnitude ( $M_V = -18.58 \pm 0.17$  mag) is also brighter than the majority of SNe IIb ( $\sim -17.5$  mag), apart from overluminous SN 2018gk and DES14X2fna. After the explosion, the light curves in the Vriz-bands show a linear decline after peak, and the other bands follow a similar trend starting approximately 40 days after their respective peaks. Spectroscopic monitoring of SN 2017ckj spanned ~140 days, providing a comprehensive optical dataset from early light to the onset of the nebular phase. The earliest spectrum, obtained at +3.0 d, exhibits flash-ionized features of H $\alpha$  and He II, along with the blue featureless continuum. During the intermediate phase, the spectra develop prominent P-Cygni profiles of H $\alpha$  and He I, similar to SN 2018gk. The late-time spectrum at +138.9 d displays a strong H $\alpha$ -like emission profile while [O1] feature remains weak. In comparison, in the spectra of prototypical SN 1993J, the H $\alpha$  feature weakens and becomes fainter than [O1] features at the same stage. Unfortunately, SN 2017ckj became too faint to be observed further due to its large distance of  $158 \pm 11$  Mpc. To explain the peculiar light curve evolution and the late-time distinct  $H\alpha$  profile at the last +138.9 d spectrum, we considered that the progenitor of SN 2017ckj likely possesses a massive H-rich envelope of  $0.4^{+0.1}_{-0.1} M_{\odot}$  and a high <sup>56</sup>Ni mass of  $0.21^{+0.05}_{-0.03} M_{\odot}$ .

Several ongoing and upcoming high-resolution surveys are expected to significantly enhance our understanding of the progenitors and explosion mechanisms of SNe. Looking ahead, the Vera Rubin Observatory's Legacy Survey of Space and Time (LSST) is expected to detect faint sources down to  $r \sim 27.5$  mag and discover up to 10 million SNe over its nominal 10-year mission (Simongini et al. 2025). Meanwhile, the China Space Station Telescope (CSST), a serviceable two-meter-aperture widefield telescope, is expected to provide over 16000 well-classified SN candidates, and its near-ultraviolet observations of CSST are anticipated to capture hundreds of shock-cooling events each year (Liu et al. 2024). With the increasing availability of deep, high-cadence survey data, these large-scale telescope observations will provide critical insights into the diverse origins and evolutionary pathways of SNe.

# Data availability

Photometric data for this SN IIb presented in this study are available at the CDS via ..... Our observations are available via the Weizmann Interactive Supernova Data Repository (WISeREP; Yaron & Gal-Yam 2012)

#### References

Abdurro'uf, Accetta, K., Aerts, C., et al. 2022, ApJS, 259, 35 Albareti, F. D., Allende Prieto, C., Almeida, A., et al. 2017, ApJS, 233, 25 Aldering, G., Humphreys, R. M., & Richmond, M. 1994, AJ, 107, 662 Arcavi, I., Hosseinzadeh, G., Brown, P. J., et al. 2017, ApJ, 837, L2 Arnett, W. D. & Fu, A. 1989, ApJ, 340, 396 Barbon, R., Benetti, S., Cappellaro, E., et al. 1995, A&AS, 110, 513 Benetti, S. 2017, Transient Name Server Classification Report, 2017-373, 1 Bersten, M. C., Benvenuto, O. G., Nomoto, K., et al. 2012, ApJ, 757, 31 Bersten, M. C., Folatelli, G., García, F., et al. 2018, Nature, 554, 497 Bose, S., Dong, S., Kochanek, C. S., et al. 2021, MNRAS, 503, 3472 Branch, D., Benetti, S., Kasen, D., et al. 2002, ApJ, 566, 1005 Branch, D. & Wheeler, J. C. 2017, Supernova Explosions (Cambridge University

Brown, P. J., Breeveld, A. A., Holland, S., Kuin, P., & Pritchard, T. 2014, Ap&SS, 354, 89

Cappellaro, E. 2014, SNOoPy: a package for SN photometry, http://

sngroup.oapd.inaf.it/snoopy.html

Cardelli, J. A., Clayton, G. C., & Mathis, J. S. 1989, ApJ, 345, 245 Chambers, K. C., Magnier, E. A., Metcalfe, N., et al. 2016, arXiv e-prints, arXiv:1612.05560

Charalampopoulos, P., Kotak, R., Sollerman, J., et al. 2025, arXiv e-prints, arXiv:2506.12135

Chevalier, R. A. & Soderberg, A. M. 2010, ApJ, 711, L40 Chornock, R., Filippenko, A. V., Li, W., et al. 2011, ApJ, 739, 41 Clocchiatti, A. & Wheeler, J. C. 1997, ApJ, 491, 375

Clocchiatti, A., Wheeler, J. C., Benetti, S., & Frueh, M. 1996, ApJ, 459, 547 Crockett, R. M., Eldridge, J. J., Smartt, S. J., et al. 2008, MNRAS, 391, L5

Cutri, R. M., Wright, E. L., Conrow, T., et al. 2013, Explanatory Supplement to the AllWISE Data Release Products, Explanatory Supplement to the All-WISE Data Release Products, by R. M. Cutri et al.

Desai, D. D., Ashall, C., Shappee, B. J., et al. 2023, MNRAS, 524, 767 Dessart, L., John Hillier, D., & Sarangi, A. 2025, A&A, 698, A293

Dong, Y., Valenti, S., Ashall, C., et al. 2024, ApJ, 974, 316

Drake, G. 2006, in Springer Handbook of Atomic, ed. G. W. F. Drake (Springer-Verlag), 199

Drout, M. R., Soderberg, A. M., Gal-Yam, A., et al. 2011, ApJ, 741, 97 Eldridge, J. J., Fraser, M., Smartt, S. J., Maund, J. R., & Crockett, R. M. 2013, MNRAS, 436, 774

Elmhamdi, A., Danziger, I. J., Cappellaro, E., et al. 2004, A&A, 426, 963 Ergon, M., Jerkstrand, A., Sollerman, J., et al. 2015, A&A, 580, A142 Ergon, M., Lundqvist, P., Fransson, C., et al. 2024, A&A, 683, A241 Ergon, M., Sollerman, J., Fraser, M., et al. 2014, A&A, 562, A17 Ertl, T., Woosley, S. E., Sukhbold, T., & Janka, H. T. 2020, ApJ, 890, 51

Fang, Q., Maeda, K., Kuncarayakti, H., Sun, F., & Gal-Yam, A. 2019, Nature Astronomy, 3, 434

Ferrari, L., Folatelli, G., Ertini, K., Kuncarayakti, H., & Andrews, J. E. 2024, A&A, 687, L20

Filippenko, A. V. 1988, AJ, 96, 1941

Filippenko, A. V. & Matheson, T. 2003, arXiv e-prints, astro

Fisher, A., Branch, D., Nugent, P., & Baron, E. 1997, ApJ, 481, L89

Folatelli, G., Bersten, M. C., Kuncarayakti, H., et al. 2015, ApJ, 811, 147

Fransson, C. & Chevalier, R. A. 1987, ApJ, 322, L15 Fransson, C. & Chevalier, R. A. 1989, ApJ, 343, 323

Fransson, C., Lundqvist, P., & Chevalier, R. A. 1996, ApJ, 461, 993 Fremling, C., Sollerman, J., Kasliwal, M. M., et al. 2018, A&A, 618, A37 Gal-Yam, A., Arcavi, I., Ofek, E. O., et al. 2014, Nature, 509, 471

Gangopadhyay, A., Maeda, K., Singh, A., et al. 2023, ApJ, 957, 100

Gangopadhyay, A., Misra, K., Pastorello, A., et al. 2018, MNRAS, 476, 3611

Gilkis, A. & Arcavi, I. 2022, MNRAS, 511, 691

Gräfener, G. & Vink, J. S. 2016, MNRAS, 455, 112

Grayling, M., Gutiérrez, C. P., Sullivan, M., et al. 2021, MNRAS, 505, 3950 Hachinger, S., Mazzali, P. A., Taubenberger, S., et al. 2012, MNRAS, 422, 70

Heger, A., Fryer, C. L., Woosley, S. E., Langer, N., & Hartmann, D. H. 2003, ApJ, 591, 288

Hosseinzadeh, G., Bostroem, K. A., Ben-Ami, T., & Gomez, S. 2024, Light Curve Fitting v0.10.0

Hosseinzadeh, G., Farah, J., Shrestha, M., et al. 2023, ApJ, 953, L16 Hosseinzadeh, G., Kilpatrick, C. D., Dong, Y., et al. 2022, ApJ, 935, 31 Hosseinzadeh, G., Valenti, S., McCully, C., et al. 2018, ApJ, 861, 63

Huang, X.-B., Wang, X.-G., Li, L., et al. 2024, ApJ, 970, 103

Jerkstrand, A., Fransson, C., Maguire, K., et al. 2012, A&A, 546, A28 Jerkstrand, A., Smartt, S. J., Fraser, M., et al. 2014, MNRAS, 439, 3694

Jordi, K., Grebel, E. K., & Ammon, K. 2006, A&A, 460, 339

Kilpatrick, C. D., Coulter, D. A., Foley, R. J., et al. 2022, ApJ, 936, 111 Kilpatrick, C. D., Foley, R. J., Abramson, L. E., et al. 2017, MNRAS, 465, 4650 Kochanek, C. S. 2019, MNRAS, 483, 3762

Kumar, B., Pandey, S. B., Sahu, D. K., et al. 2013, MNRAS, 431, 308 Landolt, A. U. 1992, AJ, 104, 340

Liu, C., Xu, Y., Meng, X., et al. 2024, Science China Physics, Mechanics, and Astronomy, 67, 119512

Liu, Y.-Q., Modjaz, M., Bianco, F. B., & Graur, O. 2016, ApJ, 827, 90

Maeda, K., Hattori, T., Milisavljevic, D., et al. 2015, ApJ, 807, 35

Maeda, K., Katsuda, S., Bamba, A., Terada, Y., & Fukazawa, Y. 2014, ApJ, 785,

Marion, G. H., Vinko, J., Kirshner, R. P., et al. 2014, ApJ, 781, 69

Matheson, T., Filippenko, A. V., Barth, A. J., et al. 2000, AJ, 120, 1487 Matheson, T., Filippenko, A. V., Li, W., Leonard, D. C., & Shields, J. C. 2001, AJ, 121, 1648

Maund, J. R., Fraser, M., Ergon, M., et al. 2011, ApJ, 739, L37

Maund, J. R., Smartt, S. J., Kudritzki, R. P., Podsiadlowski, P., & Gilmore, G. F. 2004, Nature, 427, 129

Mazzali, P. A., Kawabata, K. S., Maeda, K., et al. 2005, Science, 308, 1284 Medler, K., Mazzali, P. A., Teffs, J., et al. 2022, MNRAS, 513, 5540

Morales-Garoffolo, A., Elias-Rosa, N., Bersten, M., et al. 2015, MNRAS, 454,

Nagy, A. P. & Vinkó, J. 2016, A&A, 589, A53

Nakar, E. & Piro, A. L. 2014, ApJ, 788, 193

Nicholl, M. 2018, Research Notes of the American Astronomical Society, 2, 230 Niemela, V. S., Ruiz, M. T., & Phillips, M. M. 1985, ApJ, 289, 52

Niu, Z., Sun, N.-C., & Liu, J. 2024, ApJ, 970, L9 Niu, Z., Sun, N.-C., Maund, J. R., et al. 2025, ApJ, 987, L10

Ouchi, R. & Maeda, K. 2017, ApJ, 840, 90
Pastorello, A., Kasliwal, M. M., Crockett, R. M., et al. 2008, MNRAS, 389, 955 Pessi, P. J., Folatelli, G., Anderson, J. P., et al. 2019, MNRAS, 488, 4239 Podsiadlowski, P. 1992, PASP, 104, 717

Prentice, S. J. & Mazzali, P. A. 2017, MNRAS, 469, 2672

Prentice, S. J., Mazzali, P. A., Pian, E., et al. 2016, MNRAS, 458, 2973

Puls, J., Vink, J. S., & Najarro, F. 2008, A&A Rev., 16, 209

Reguitti, A., Pastorello, A., Smartt, S. J., et al. 2025, A&A, 698, A129 Richmond, M. W., Treffers, R. R., Filippenko, A. V., & Paik, Y. 1996, AJ, 112,

Richmond, M. W., Treffers, R. R., Filippenko, A. V., et al. 1994, AJ, 107, 1022

Ripero, J., Garcia, F., Rodriguez, D., et al. 1993, IAU Circ., 5731, 1 Sahu, D. K., Anupama, G. C., & Chakradhari, N. K. 2013, MNRAS, 433, 2 Sapir, N. & Waxman, E. 2017, ApJ, 838, 130

Schlafly, E. F. & Finkbeiner, D. P. 2011, ApJ, 737, 103

Shingles, L., Smith, K. W., Young, D. R., et al. 2021, Transient Name Server AstroNote, 7, 1

Simongini, A., Ragosta, F., Di Palma, I., & Piranomonte, S. 2025, arXiv e-prints, arXiv:2506.04184

Smartt, S. J. 2009, ARA&A, 47, 63

Smith, K. W., Smartt, S. J., Young, D. R., et al. 2020, PASP, 132, 085002 Smith, N. 2014, ARA&A, 52, 487

Smith, N., Li, W., Filippenko, A. V., & Chornock, R. 2011, MNRAS, 412, 1522

Spergel, D. N., Bean, R., Doré, O., et al. 2007, ApJS, 170, 377 Sravan, N., Marchant, P., & Kalogera, V. 2019, ApJ, 885, 130

Storey, P. J. & Hummer, D. G. 1995, MNRAS, 272, 41 Stritzinger, M. D., Anderson, J. P., Contreras, C., et al. 2018, A&A, 609, A134 Subrayan, B. M., Sand, D. J., Bostroem, K. A., et al. 2025, arXiv e-prints, arXiv:2505.02908

Tartaglia, L., Fraser, M., Sand, D. J., et al. 2017, ApJ, 836, L12

Taubenberger, S., Navasardyan, H., Maurer, J. I., et al. 2011, MNRAS, 413, 2140 Temaj, D., Schneider, F. R. N., Laplace, E., Wei, D., & Podsiadlowski, P. 2024, A&A, 682, A123

Thielemann, F.-K., Nomoto, K., & Hashimoto, M.-A. 1996, ApJ, 460, 408 Tody, D. 1986, in Proc. SPIE, Vol. 627, Instrumentation in astronomy VI, ed. D. L. Crawford, 733

Tody, D. 1993, in Astronomical Society of the Pacific Conference Series, Vol. 52, Astronomical Data Analysis Software and Systems II, ed. R. J. Hanisch, R. J. V. Brissenden, & J. Barnes, 173

Tomasella , L., Benetti, S., Cappellaro, E., et al. 2014, Astronomische Nachrichten, 335, 841

Tomasella, L., Benetti, S., Cappellaro, E., et al. 2017, The Astronomer's Telegram, 10219, 1

Tonry, J., Stalder, B., Denneau, L., et al. 2017, Transient Name Server Discovery Report, 2017-355, 1

Tonry, J. L., Denneau, L., Flewelling, H., et al. 2018a, ApJ, 867, 105

Tonry, J. L., Denneau, L., Heinze, A. N., et al. 2018b, PASP, 130, 064505

Tsang, B. T. H., Kasen, D., & Bildsten, L. 2022, ApJ, 936, 28

- Tsvetkov, D. Y., Volkov, I. M., Baklanov, P., Blinnikov, S., & Tuchin, O. 2009, Peremennye Zvezdy, 29, 2
- Tsvetkov, D. Y., Volkov, I. M., Sorokina, E. I., et al. 2012, Photometric observations and preliminary modeling of type IIb supernova 2011dh
- Van Dyk, S. D., Garnavich, P. M., Filippenko, A. V., et al. 2002, PASP, 114, 1322

Van Dyk, S. D., Li, W., Cenko, S. B., et al. 2011, ApJ, 741, L28

Van Dyk, S. D., Zheng, W., Fox, O. D., et al. 2014, AJ, 147, 37

Wheeler, J. C., Johnson, V., & Clocchiatti, A. 2015, MNRAS, 450, 1295

Woosley, S. E., Eastman, R. G., Weaver, T. A., & Pinto, P. A. 1994, ApJ, 429, 300

Woosley, S. E. & Weaver, T. A. 1995, ApJS, 101, 181

Yaron, O. & Gal-Yam, A. 2012, PASP, 124, 668

Yaron, O., Perley, D. A., Gal-Yam, A., et al. 2017, Nature Physics, 13, 510

Yoon, S.-C. & Cantiello, M. 2010, ApJ, 717, L62

Yoon, S.-C., Dessart, L., & Clocchiatti, A. 2017, ApJ, 840, 10

Zou, X., Kumar, B., Singh Teja, R., et al. 2025, arXiv e-prints, arXiv:2505.19831

- Yunnan Observatories, Chinese Academy of Sciences, Kunming 650216, China
- <sup>2</sup> International Centre of Supernovae, Yunnan Key Laboratory, Kunming 650216, China
- <sup>3</sup> University of Chinese Academy of Sciences, Beijing 100049, China
- <sup>4</sup> INAF Osservatorio Astronomico di Padova, Vicolo dell'Osservatorio 5, 35122 Padova, Italy
- <sup>5</sup> Institute of Space Sciences (ICE, CSIC), Campus UAB, Carrer de Can Magrans, s/n, E-08193 Barcelona, Spain
- <sup>6</sup> INAF Osservatorio Astronomico d'Abruzzo, Via Mentore Maggini Snc, 64100 Teramo, Italy
- <sup>7</sup> School of Physics, O'Brien Centre for Science North, University College Dublin, Belfield, Dublin 4, Ireland
- 8 Astronomical Observatory, University of Warsaw, Al. Ujazdowskie 4. 00-478 Warszawa, Poland
- <sup>9</sup> Department of Physics and Astronomy, University of Turku, FI-20014 Turku, Finland
- Fabra Observatory, Royal Academy of Sciences and Arts of Barcelona (RACAB), 08001 Barcelona, Spain
- <sup>11</sup> Institute for Space Studies of Catalonia (IEEC), Campus UPC, 08860 Castelldefels (Barcelona), Spain
- Finnish Centre for Astronomy with ESO (FINCA), University of Turku, Vesilinnantie 5, Quantum 20014 Turku, Finland
- The Oskar Klein Centre, Department of Astronomy, Stockholm University, AlbaNova, SE-10691 Stockholm, Sweden
- <sup>14</sup> School of Sciences, European University Cyprus, Diogenes Street, Engomi, 1516 Nicosia, Cyprus
- <sup>15</sup> Physics and Astronomy Department Galileo Galilei, University of Padova, Vicolo dell'Osservatorio 3, I-35122, Padova, Italy
- School of Electronic Science and Engineering, Chongqing University of Posts and Telecommunications, Chongqing 400065, P.R. China
- <sup>17</sup> INAF Osservatorio Astronomico di Brera, Via E. Bianchi 46, 23807 Merate (LC), Italy
- <sup>18</sup> Cosmic Dawn Center (DAWN)
- <sup>19</sup> Niels Bohr Institute, University of Copenhagen, Jagtvej 128, 2200 København N, Denmark
- <sup>20</sup> INAF–Osservatorio Astronomico di Capodimonte, Salita Moiariello 16, 80131 Napoli, Italy
- Astrophysics Research Centre, School of Mathematics and Physics, Queen's University Belfast, Belfast BT7 1NN, UK
- <sup>22</sup> Department of Physics and Astronomy, Aarhus University, Ny Munkegade 120, DK-8000 Aarhus C, Denmark
- <sup>23</sup> School of Physics and Astronomy, Beijing Normal University, Beijing 100875, P.R. China
- <sup>24</sup> Department of Physics, Faculty of Arts and Sciences, Beijing Normal University, Zhuhai 519087, P.R. China

# Appendix A: Supplementary figure

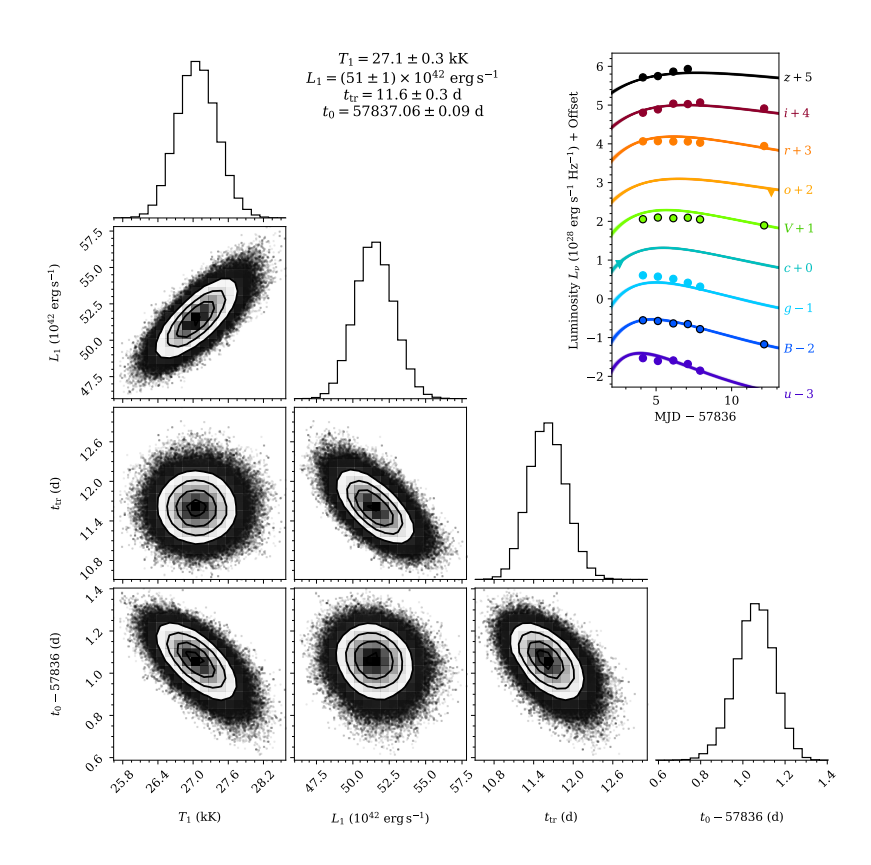


Fig. A.1: Modelling of shock-cooling light curve of SN 2017ckj using Light Curve Fitting package (Hosseinzadeh et al. 2024) based on the shock-cooling model of Sapir & Waxman (2017). The posterior probability distributions of the model parameters are shown, including the temperature 1 day after explosion ( $T_1$ ), the total luminosity 1 day after explosion ( $L_1$ ), the time at which the envelope becomes transparent ( $t_{tr}$ ), and the time of explosion ( $t_0$ ). The best-fit values of these parameters and their  $1\sigma$  credible intervals are provided at the top.

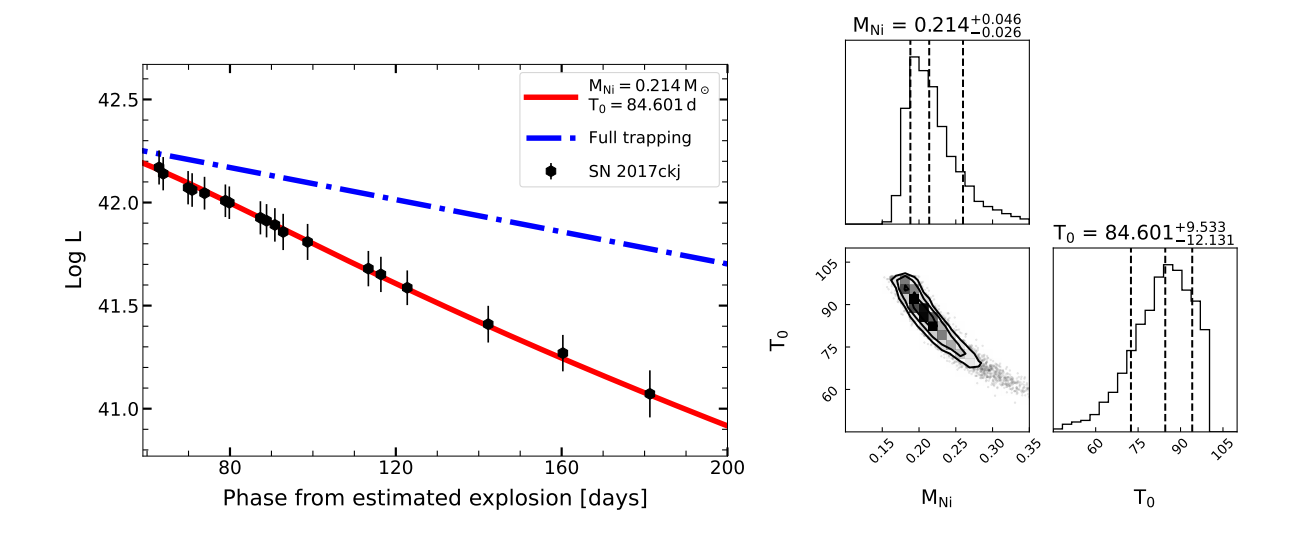


Fig. A.2: Fit of the modified radioactive decay model to the late-time full bolometric light curve of SN 2017ckj. In the left panel, the bolometric light curve fitting is shown by the red solid line, while the full  $\gamma$ -ray trapping model is presented in blue dashed-dotted line for comparison. The right panel presents the posterior distribution from MCMC sampling. The mean of the posterior distribution and  $1\sigma$  uncertainties are marked.

# Appendix B: Observations and data reduction

### Appendix B.1: Photometric data

We conducted multi-band optical (Sloan *ugriz*, Johnson-Cousins *BV*) follow-up campaigns of SN 2017ckj starting shortly after its classification. The telescopes and instruments utilised were the following: The 1.82-m Copernico Telescope atop Mount Ekar with the Asiago Faint Object Spectrograph and Camera (AFOSC), hosted by INAF – Padova Astronomical Observatory, at the Asiago site, Italy; The 2.56-m Nordic Optical Telescope (NOT) equipped with the Alhambra Faint Object Spectrograph and Camera (ALFOSC), and the 10.4-m Gran Telescopio Canarias (GTC) with Optical System for Imaging and low-Intermediate-Resolution Integrated Spectroscopy (OSIRIS), both located at Roque de los Muchachos Observatory (La Palma, Canary Islands, Spain).

The raw images were first pre-reduced by applying bias and overscan corrections, flat-fielding, and trimming, which are standard correction steps performed in IRAF<sup>4</sup> (Tody 1986, 1993). If multiple exposures were taken with the same instrument and on the same night, we combined them into stacked science frames to increase the S/N. The steps necessary to obtain the SN magnitude were performed using the dedicated pipeline snoopy<sup>5</sup> developed by Cappellaro (2014). snoopy consists of a collection of PYTHON-based scripts calling standard IRAF tasks within PYRAF. The template subtraction was adopted for ugriz-bands and BVbands of SN 2017ckj to remove the background contamination from the host galaxy. When the SN was not detected, an upper limit to the object brightness was estimated. Photometric calibration of instrumental magnitudes was performed by adopting instrumental zero points (ZPs) and colour terms (CTs) inferred through observations of standard stars on photometric nights. Specifically, Johnson-Cousins filter photometry was calibrated using standard stars from the Landolt (1992) catalogue, while Sloan-filter data were retrieved from the SDSS DR 18 catalogue (Abdurro'uf et al. 2022). To correct the instrumental ZPs on nonphotometric nights and improve the photometric calibration accuracy, we compared the average magnitudes of local sequences of standard stars in the fields of the SN to those obtained on photometric nights. With the corrected ZPs, we calibrated the SN apparent magnitudes on all nights.

We also collected photometric data from the public ATLAS sky surveys for transients. The orange (*o*) and cyan (*c*) band light curves were directly produced by the ATLAS data-release server <sup>6</sup> (Shingles et al. 2021). Panoramic Survey Telescope and Rapid Response System (Pan-STARRS) is a wide-field imaging survey system (Chambers et al. 2016) and also provides late-time photometric data, which we incorporate in this paper.

# Appendix B.2: Spectroscopic data

Spectroscopic observations of the SN 2017ckj were carried out using the following telescopes: Copernico 1.82-m/AFOSC, 2.56-m NOT/ALFOSC, and 10.4-m GTC/OSIRIS. The spectra obtained with Copernico 1.82-m/AFOSC, 2.56-m NOT/ALFOSC, and GTC/OSIRIS were reduced using the dedicated pipeline Foscgui developed by E. Cappellaro. All raw spectral data were reduced following the standard steps in IRAF<sup>7</sup> (Tody 1986, 1993). The pre-reduction steps, such as bias, over-

scan, flat-fielding correction, and trimming, are similar to those described for the imaging data. Then, the one-dimensional (1D) spectra were optimally extracted from the 2D images. Wavelength calibrations were performed using arc lamps, while flux calibrations were performed using spectrophotometric standard stars taken on the same nights. Subsequently, the strongest telluric absorption bands, such as  $O_2$  and  $H_2O$ , were removed from the SN spectra using the spectra of the standard stars. Finally, the accuracy of flux calibration for all spectra was checked against the coeval photometric data. The information on the instrumentation used for the spectroscopic observations is reported in Table C.2.

# **Appendix C: Data tables**

# Acknowledgements

We gratefully thank the anonymous referee for his/her insightful comments and suggestions that improved the paper.

This work is supported by the National Natural Science Foundation of China (Nos 12288102, 12225304, 12090040/12090043, 12303054, 12473032), the National Key Research and Development Program of China (Nos. 2021YFA1600404, 2024YFA1611603), the Western Light Project of CAS (No. XBZG-ZDSYS-202117), the Yunnan Revitalization Talent Support Program (Yunling Scholar Project), the Yunnan Revitalization Talent Support Program-Young Talent project, the Yunnan Fundamental Research Projects (Nos 202201BC070003, 202401AU070063, 202501AS070078, 202501AW070001), and the International Centre of Supernovae, Yunnan Key Laboratory (No. 202302AN360001). SB, EC, NER, PO, AP, AR, IS, LT and GV acknowledge financial support from the PRIN-INAF 2022 "Shedding light on the nature of gap transients: from the observations to the models". AR also acknowledges financial support from the GRAWITA Large Program Grant (PI P. D'Avanzo). AF acknowledges funding by the European Union - NextGenerationEU RFF M4C2 1.1 PRIN 2022 project "2022RJLWHN URKA" and by INAF 2023 Theory Grant ObFu 1.05.23.06.06 "Understanding R-process & Kilonovae Aspects (URKA)". JH acknowledges the Vilho, Yriö and Kalle Väisälä Foundation of the Finnish Academy of Science and Letters. TK acknowledges support from the Research Council of Finland project 360274. T.M.R is part of the Cosmic Dawn Center (DAWN), which is funded by the Danish National Research Foundation under grant DNRF140. T.M.R acknowledges support from the Research Council of Finland project 350458. S.M. acknowledges financial support from the Research Council of Finland project 350458. We thank S. Taubenberger for conducting the template observations with the Copernico Telescope. We thank Jingxiao Luo, Xinbo Huang and Zeyi Zhao for helpful discussions and valuable suggestions.

Based on observations collected with the AFOSC instrument at the 1.82-m Copernico Telescope of the INAF – Osservatorio Astronomico di Padova (Asiago, Italy). We thank the technical staff of the Asiago Observatory for their support during the observations. The data in this study include observations made with the Nordic Optical Telescope, owned in collaboration by the University of Turku and Aarhus University and operated jointly by Aarhus University, the University of Turku, and the University of Oslo, representing Denmark, Finland, and Norway; the University of Iceland; and Stockholm University at the Observatorio del Roque de los Muchachos, La Palma, Spain, of the Instituto de Astrofisica de Canarias. The data presented here were obtained in part with ALFOSC, which is pro-

<sup>4</sup> https://iraf-community.github.io/

<sup>5</sup> http://sngroup.oapd.inaf.it/snoopy.html/

<sup>6</sup> https://fallingstar-data.com/forcedphot/

<sup>7</sup> http://iraf.noao.edu/

L.-H. Li et al.: SN 2017ckj

Table C.1: Properties of the comparison SNe IIb.

SN IIb	Explosion Date	Redshift	Distance	$E(B-V)_{Gal}$	$E(B-V)_{Host}$	References
	[MJD]	Z	[Mpc]	[mag]	[mag]	
1993J	49072.0	-0.000113	2.9	0.069	0.11	1,2,3
2008ax	54528.8	0.00456	$9.6 \pm 1.3$	0.022	0.278	4,5,6
2011dh	55712.5	0.001638	$8.03 \pm 0.77$	0.03	0.04	7,8,9
2011fu	55824.5	0.001845	$74.5 \pm 5.2$	0.068	0.035	10
2013cu	56414.93	0.025734	108	0.0105	0	11
DES14X2fna	56927.7	0.0453	$200.7 \pm 3.0$	0.0225	0	12
2015as	57332.0	0.0036	19.2	0.008	0	13
2016gkg	57651.2	0.0049	21.8	0.0166	0.09	14,15
2018gk / ASASSN-18am	58130.1	0.031010	$140.5 \pm 2.3$	0.0086	0	16
2019tua	58785.3	0.010	41.39	0.06	0	17
2020acat	59192.0	0.007932	$35.3 \pm 4.4$	0.0207	0	18
2021bxu	59246.3	0.0178	72±5	0.014	0	19
2017ckj	57836.6	0.037	158.1±11.1	0.013	0	This work

References: 1. Richmond et al. (1994), 2. Barbon et al. (1995), 3. Richmond et al. (1996), 4. Pastorello et al. (2008), 5. Tsvetkov et al. (2009), 6. Taubenberger et al. (2011), 7. Tsvetkov et al. (2012), 8. Sahu et al. (2013), 9. Ergon et al. (2014), 10. Morales-Garoffolo et al. (2015), 11. Gal-Yam et al. (2014), 12. Grayling et al. (2021), 13. Gangopadhyay et al. (2018), 14. Arcavi et al. (2017), 15. Bersten et al. (2018), 16. Bose et al. (2021), 17. Huang et al. (2024), 18. Medler et al. (2022), 19. Desai et al. (2023).

Table C.2: Log of spectroscopic observations of SN 2017ckj.

Date	MJD	Phase <sup>a</sup>	Telescope+Instrument	Grism/Grating+Slit	Spectral range	Resolution	Exp. time
		(days)			(Å)	(Å)	(s)
20170328	57840.1	+3.0	Copernico+AFOSC	gr04+1.69"	2890-7950	16	1800
20170329	57841.1	+4.0	Copernico+AFOSC	vph7+1.69"	3230-8950	16	1800
20170330	57842.2	+5.1	Copernico+AFOSC	vph7+1.69"	3470-7030	16	1800
20170331	57843.1	+6.0	Copernico+AFOSC	vph7+1.69"	3290-7030	16	1800
20170405	57848.1	+11.0	NOT+ALFOSC	gm4+1.0"	3460-9310	12	1800
20170422	57865.2	+28.1	NOT+ALFOSC	gm4+1.3"	3660-9310	14	2400
20170506	57879.0	+41.9	NOT+ALFOSC	gm4+1.0"	3660-9300	12	3600
20170531	57904.1	+67.0	NOT+ALFOSC	gm4+1.0"	3760-9410	12	3600
20170627	57931.0	+93.9	NOT+ALFOSC	gm4+1.0"	3660-9360	12	2700
20170715	57950.0	+112.9	GTC+OSIRIS	R1000B/R1000R+1.0"	3750-10020	8	1800
20170810	57976.0	+138.9	GTC+OSIRIS	R300B/R300R+1.0"	3880-10260	7	1800

<sup>&</sup>quot;Phases are relative to the estimated explosion epoch (MJD =  $57837.1 \pm 0.1$ ) in observer frame.

vided by the Instituto de Astrofísica de Andalucía (IAA) under a joint agreement with the University of Copenhagen and NOT. This work is based on observations made with the Gran Telescopio Canarias (GTC), installed in the Spanish Observatorio del Roque de los Muchachos (ORM) of the Instituto de Astrofísica de Canarias (IAC), using the OSIRIS instrument. This work has made use of data from the Asteroid Terrestrial-impact Last Alert System (ATLAS) project. The ATLAS project is primarily funded to search for near earth asteroids through NASA grants NN12AR55G, 80NSSC18K0284, and 80NSSC18K1575; byproducts of the NEO search include images and catalogs from the survey area. The ATLAS science products have been made possible through the contributions of the University of Hawaii Institute for Astronomy, the Queen's University Belfast, the Space Telescope Science Institute, the South African Astronomical Observatory, and The Millennium Institute of Astrophysics (MAS), Chile. This work has made use of data from the Pan-STARRS1 Surveys (PS1) and the PS1 public science archive. The PS1 and the PS1 public science archive have been made possible through contributions by the Institute for Astronomy, the University of Hawaii, the Pan-STARRS Project Office, the Max-Planck Society and its participating institutes, the Max Planck Institute for Astronomy, Heidelberg and the Max Planck Institute for Extraterrestrial Physics, Garching, The Johns Hopkins University, Durham University, the University of Edinburgh, the Queen's University Belfast, the Harvard-Smithsonian Center for Astrophysics, the Las Cumbres Observatory Global Telescope Network Incorporated, the National Central University of Taiwan, the Space Telescope Science Institute, the National Aeronautics and Space Administration under Grant No. NNX08AR22G issued through the Planetary Science Division of the NASA Science Mission Directorate, the National Science Foundation Grant No. AST-1238877, the University of Maryland, Eotvos Lorand University (ELTE), the Los Alamos National Laboratory, and the Gordon and Betty Moore Foundation. This research has made use of the NASA/IPAC Extragalactic Database (NED), which is operated by the Jet Propulsion Laboratory, California Institute of Technology, under contract with the National Aeronautics and Space Administration. iraf was distributed by the National Optical Astronomy Observatory, which was managed by the Association of Universities for Research in Astronomy (AURA), Inc., under a cooperative agreement with the U.S. NSF.